



Numerical modeling of plastic deformation and failure around a wellbore in compaction and dilation modes

Aboozar Garavand^{1,2}  | Yuri Pavlovich Stefanov^{3,4} |
Yuri Leonidovich Rebetsky⁵ | Rustam Alfredovich Bakeev^{4,3} |
Artem Veniaminovich Myasnikov²

¹Gubkin Russian State University of Oil and Gas, Moscow, Russia

²Skolkovo Institute of Science and Technology (Skoltech), Moscow, Russia

³Trofimuk Institute of Petroleum Geology and Geophysics, SB RAS (IPGG SB RAS), Novosibirsk, Russia

⁴Institute of Strength Physics and Materials Science, SB RAS (ISPMS SB RAS), Tomsk, Russia

⁵Schmidt Institute of Physics of the Earth of RAS (IPE RAS), Moscow, Russia

Correspondence

Aboozar Garavand, Gubkin Russian State University of Oil and Gas, Moscow, Russia.

Email: A.Garavand@Skoltech.ru

Summary

In many wellbore stability analyses, the ability to forecast both the occurrence and extent of plastic deformation and failure hinges upon a fundamental understanding of deformation mode and failure mechanism in the reservoir rock. This study focuses on analyzing plastic zones, localized deformations, and failures around a borehole drilled overbalanced or underbalanced through a highly porous rock formation. Based on several laboratory experiments, porous rocks are prone to deform under both shear-induced dilation and shear-enhanced compaction mechanisms depending on the stress state. The shapes of the deformation and failure patterns around the borehole are shown, depending on the initial stress state and the local stress paths. The inquiry of the local stress paths in the near-wellbore zone facilitates the understanding of the reasons for different types of failure mechanisms, including the mixed-mode and the plastic deformation structures. The modification of the 2D plane strain condition by imitating third stress in the numerical scheme helps us bring the stress paths closer to the real state of loading conditions. Our modeling reveals that the transition from isotropic to anisotropic stress state is accompanied by an increase in the deviatoric part of effective shear tensor that leads to the development of inelastic deformation, degradation, and subsequent rock failure. Particular interest is devoted to the modeling of strain localization especially in compaction mode around a wellbore and computing the amount of stress concentration at the tips of dog-eared breakouts. Stress concentration can result in a change in irreversible deformation mode from dilatancy to compaction, elucidating the formation of the shear-enhanced compaction phenomenon at the failure tips in the direction of the minimum horizontal stress.

KEYWORDS

compaction localization, failure mechanism, local stress path, modified 2D plane strain, plastic deformation, wellbore stability

1 | INTRODUCTION

Underground formations are subject to in situ stresses from the weight of overlying layers and lateral confinements. The stress state of the formation is in the equilibrium state until being altered by a drilling operation. Such alteration in stress state and pore pressure causes stress concentration around the wellbore, which may exceed the rock strength and consequently lead to borehole failure. Therefore, maintaining wellbore stability requires a supportive pressure, which is provided by the drilling fluid. Among numerous published models for wellbore stability analysis, the linear elastic model (LEM) is the most conventional approach due to its simplicity and minimal input parameters.¹⁻⁷ The LEM models assume that the failure of rocks occurs in shear mode and are merely able to predict rough estimation of the failure zone. However, such an analysis does not allow us to describe the state of the medium and the deformation process beyond the yield surface. In fact, they only focus on the elastic yield limit.

Moreover, experiments and field observations show that LEM models do not adequately depict the behavior of unconsolidated and high porosity formations. Several laboratory experiments show the occurrence of plastic (inelastic) deformation either in shear or compaction mode with a subsequent rock failure.⁸⁻¹⁷ Alternatively, numerical elastoplastic models offer the ability to overcome the inaccuracies of LEM in dealing with these types of formations.

There are several semi-analytical elastoplastic solutions made plausible by adopting a complex variable theory and a conformal transformation technique in conjunction with both Tresca and Mohr-Coulomb failures criteria.¹⁸⁻²³ However, the application of these models is restricted in petroleum applications due to the assumptions made to find the solution. Later on, Fung et al²⁴ proposed an advanced elastoplastic model for borehole stability analysis in unconsolidated formation without considering the pore pressure distribution and the possible occurrence of compaction localization regions.

Unlike low porosity rocks whose strength increases with an increase in effective mean pressure and their behavior can be described by the Mohr-Coulomb, Mogi-Coulomb, or Drucker-Prager yield surfaces, porous rocks exhibit a decrease in strength with an increase in effective mean pressure above a specific value, and the yield surface has a closed cap shape.^{25,26} Dimaggio et al²⁷ proposed a model based on the combination of the Drucker-Prager yield surface in the zone of shear deformation and cap surface in the compaction zone. Moreover, in recent years, several constitutive models based on various approaches have been suggested with different intricacy levels.^{9,28-30}

Plastic potential also is an essential part of the elastoplastic modeling and is responsible for the beyond yield delineation of rock deformation. The application of associated flow rule in which the yield surface is used as plastic potential consequently results in disagreement with experimental data due to the imputation of the dilatancy coefficient to the internal friction angle. Moreover, the use of a non-associated flow rule allows a more accurate description of inelastic deformation, although it requires the construction of an independent potential function with additional parameters and measurements, which is still a very complex question in studying and modeling the rock's behavior. However, most of the studies focus on the analysis of constitutive relations and interpretation of experimental observations without paying much attention to the modeling of inelastic deformation of the real features, like oil and gas wells.

In several studies based on numerical modeling, interesting results were obtained for the development of inelastic deformation in rock samples on core-scale using the finite element method (FEM) with the weak discontinuity³¹ and strong discontinuity approaches.^{32,33} Simulation of plastic deformation in granular materials was also demonstrated using the discrete element method (DEM) or a hierarchical coupling between the FEM and DEM.³⁴⁻³⁷ However, currently, there are still many questions regarding the simulation of inelastic processes, the development of strain localization, and the failure of the geomaterials around a borehole in the petroleum industry, especially in compaction mode. Although there are numerous works with different complexity in the modeling of elastoplastic deformation in which many important features of deformation processes are shown, in practice simple models, obtained based on the elastic solution, are mainly used.

Here, an elastoplastic model with a non-associated flow rule using the combined yield surfaces is used for wellbore stability analysis. The plastic deformation is simulated by dynamic equations, which are typically used for wave propagation problems. The hardening of the medium from either shear or compaction mode is followed by the degradation (softening) process. The main goal of the work is to show the necessity of taking into account the possibility of development of irreversible deformation in different modes: dilatancy and compaction in the analysis of the wellbore stability and also to demonstrate the possibility of describing these processes through a relatively simple model. For this purpose, the effect of stress state on the development of irreversible deformation and the formation of localization zones with allowance for dilatancy and compaction under realistic loading conditions and rock parameters is considered.

2 | MATHEMATICAL MODELS OF POROUS ROCKS

To provide a consistent theory for the investigation of elastoplastic problems, it is assumed that the effective stress, σ'_{ij} , is representative of the mechanical response of the porous medium. The effective stress is defined as³⁸⁻⁴¹

$$\sigma'_{ij} = \sigma_{ij} + \alpha_B P_p \delta_{ij}, \quad (1)$$

where α_B is the Biot's coefficient, P_p is the pore pressure distribution, σ_{ij} is the total stress, and δ_{ij} is the Kronecker delta. The sign convention of the classical mechanics is adopted so that negative stress corresponds to compression and positive to tension. Assuming infinite-acting reservoir, the pore pressure distribution is governed by the linear diffusion equation⁴² solved by the Carslaw et al⁴³ as follows:

$$P_p(r, t) = P_w + \frac{2(P_w - P_0)}{\pi} \int_0^\infty \frac{J_0(xr)Y_0(xR_w) - Y_0(xr)J_0(xR_w) dx}{\exp\left(\frac{kx^2 t}{\phi\mu c_t}\right) (J_0^2(xR_w) + Y_0^2(xR_w)) x}, \quad (2)$$

where P_w is the wellbore pressure and P_0 is the initial pore pressure, $J_0(x)$ and $Y_0(x)$ are the Bessel functions of the first and second kinds, $R_w, r, t, \kappa, \phi, \mu, c_t$ are wellbore radius, radius of investigation, time, permeability, porosity, fluid viscosity, and total fluid compressibility, respectively. The pore pressure distribution is usually computed by the reservoir simulators. More accurate results can be obtained by incorporating the change in porosity and permeability by solving the coupled poro-elastoplastic model, which is quite difficult and requires large computational costs. However, it can be assumed that, in a short time interval immediately after drilling, solution (2) remains valid.

Beyond the elastic limit during the irreversible (plastic) deformation in low porosity rocks, the microcracks evolution accompanied by an increase in volume (dilatancy) and their accumulation will lead to the formation of a failure plane or localized zone. In porous rocks, the plastic deformation can involve both dilatation and compaction depending on the level of effective mean pressure. Based on effective mean pressure (stress) range, for any porous rock, there are three distinct zones with qualitatively different behavior as

1. Low effective mean pressures with the possibility of tensile stress development and subsequent creation of tensile fractures.
2. Low to intermediate effective mean pressures in which shear deformation is accompanied by dilation and increase in rock porosity: Increase in the effective mean pressure results in an increase in shear strength. The behavior of rock can be explained by the Drucker-Prager or Mohr-Coulomb models in conjunction with a non-associated flow rule.⁴⁴⁻⁴⁷
3. High effective mean pressures in which compaction deformation is accompanied by rock grains or other microstructural elements crushing with a consequent reduction in the porosity: Increase in the effective mean pressure results in the decrease in shear strength. Rudnicki⁴⁸ and Grueschow et al²⁶ gave a quite comprehensive interpretation of compaction modeling by using the elliptical cap surface.

Thus, for modeling of porous rocks in a wide loading range, the combined yield surface supporting features of all pressure ranges is required. Moreover, experiments reveal the variation of yield surface and plastic potential surface during the deformation process.^{49,50} Therefore, in addition to the shape of the initial yield surface, the variation of yield and plastic potential surfaces through time should be taken into consideration. Considering the combined model based on the truncated cone and elliptical yield surface, the conical part of the yield surface corresponds to the shear failure zone and is a modification of the Drucker-Prager model with a non-associated flow rule.^{16,51} The elliptical part corresponds to the compaction failure zone, assuming that the ellipse semi-axes depend on shear and volumetric plastic strain components.^{26,48}

Similar to the DiMaggio-Sandler model, a combined yield surface (Figure 1) of a Drucker-Prager cone constructed in the shear (plastic dilation) zone:

$$f_1 = \tau - \alpha\sigma' - c, \quad \sigma'_t \leq \sigma' < \sigma'_0 \quad (3)$$

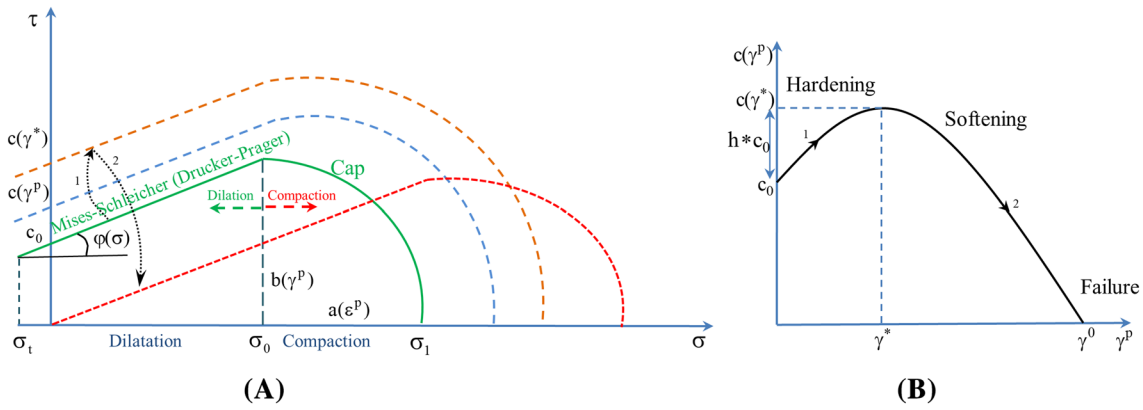


FIGURE 1 (a) Variation of the yield surface at different stages of the deformation process: The hardening of the material from either shear or compaction is followed by a decrease of cohesion and friction angle (softening); (b) strength variation during plastic deformation

and elliptical surface in the compaction zone:

$$f_2 = \frac{(\sigma' - \sigma'_0)^2}{a^2} + \frac{\tau^2}{b^2} - 1 = 0, \quad \sigma' \geq \sigma'_0 \quad (4)$$

where $\sigma' = -\sigma'_{kk}/3$ is the first effective stress invariant or effective mean pressure, $\tau = (s_{ij}s_{ij}/2)^{1/2}$ is the 2nd invariant of the stress deviator tensor, $s_{ij} = \sigma'_{ij} + \sigma'\delta_{ij}$ represents the components of the stress tensor deviator, $\alpha = \tan(\phi)$, and c are the coefficients of internal friction angle and cohesion in the Drucker-Prager cone, $a = \sigma'_1 - \sigma'_0$ and $b = c + \alpha\sigma'_0$ represent semi-axes of the ellipse, σ'_0 is the threshold effective mean pressure between shear and compaction mode (center of the ellipse), and σ'_1 is the compaction onset effective mean pressure at zero shear or grain crushing pressure. In the tensile region, the yield surface is truncated by the corresponding tensile strength σ'_t .

The yield surface variation during deformation takes place as the material hardens and softens (Figure 1). The state of the cone surface is assumed to be determined by accumulated inelastic equivalent shear strain γ^{p16} :

$$c(\gamma^p) = c_0 [1 + h(A(\gamma^p) - D(\gamma^p))], \quad (5)$$

$$A(\gamma^p) = 2(\gamma^p / \gamma^*), \quad (6)$$

$$D(\gamma^p) = (\gamma^p / \gamma^*)^2, \quad (7)$$

Here, $A(\gamma^p)$ is the linear hardening function and $D(\gamma^p)$ is the function describing damage accumulation during inelastic deformation. Thus, medium softening is associated with the accumulation of damage during the inelastic deformation. Inelastic equivalent shear strain γ^p is computed incrementally with $d\gamma^p = 2(((de_{ij})^p (de_{ij})^p)/2)^{1/2}$, $e_{ij}^p = \epsilon_{ij}^p - (1/3)\epsilon_{kk}^p \delta_{ij}$. h and γ^* are parameters describing the hardening process and the accumulated inelastic equivalent shear strain beyond which degradation begins, respectively. Based on equations (5)–(7), the complete material degradation (end of softening stage) takes place, when the accumulated inelastic equivalent shear strain reaches to $\gamma^0 = \gamma^* (1 + \sqrt{(1+h)/h})$. In other words, the material is considered completely degraded as the cohesion becomes zero (see Figure 1).

The state of the elliptical yield surface determines compaction hardening, which is assumed to be dependent upon the accumulated inelastic volumetric strain ($\epsilon^p = \epsilon_{kk}^p$). The variation of cap surface is depicted by

$$\sigma'_0(\epsilon^p) = \sigma'_0 \left(\frac{\epsilon^*}{\epsilon^* + \epsilon^p} \right)^m, \quad (8)$$

and

$$a = a_0 + r\Delta\sigma'_0, \quad (9)$$

$$b = c(\gamma^p) + \alpha\sigma'_0(\varepsilon^p), \quad (10)$$

where ε^* is the accumulated inelastic volumetric strain at the ultimate compaction and m and r are experimental parameters.

Assuming that the rock compacts only due to pore space reduction, equation (8) converts to

$$\sigma'_0(\phi) = \sigma'_0(\phi^*/\phi)^m, \quad (11)$$

where $\varepsilon^* = \phi^*$, $\Delta\phi = \varepsilon^p$, ϕ^* , and ϕ are the initial and the current porosity of the rock. When describing cap surface variation and compaction hardening by the hyperbolic function (11), infinite cap expansion occurs when porosity approaches zero. It can be justified by stating that a plastic deformation with zero porosity can only be developed in shear mode.

The last equation describing inelastic deformation is related to plastic potential function. The plastic potential function is described as follows:

$$g = \tau - \beta\sigma', \quad (12)$$

where $\beta = d\varepsilon^p/d\gamma^p$, is the dilatancy coefficient that is the volumetric strain increment to shear strain increment ratio and $\psi = \tan^{-1}(\beta)$ is the dilatancy angle, which is the slope of the plastic potential surface. The dilatancy coefficient in the proposed model is defined in terms of a stress-dependent multiplier, which is a power-law function of effective mean pressure:

$$\begin{aligned} \beta(\sigma', \varepsilon^p) &= \beta_0 \left(\frac{\sigma'_0(\varepsilon^p) - \sigma'}{\sigma'_0(\varepsilon^p)} \right)^{n_1} & \text{at } \sigma' < \sigma'_0, \\ \beta(\sigma', \varepsilon^p) &= - \left(\frac{\sigma' - \sigma'_0(\varepsilon^p)}{\sigma'_1 - \sigma'_0(\varepsilon^p)} \right)^{n_2} & \text{at } \sigma'_0 \leq \sigma' < \sigma'_1. \end{aligned} \quad (13)$$

Equation (13) defines a gradual reduction of the plastic potential surface from maximum dilatancy β_0 , which occurs at low effective mean pressures, passing through the moderate levels, zero value at the top of the yield surface, ie, $\sigma' = \sigma'_0$, going to negative dilatancy values happening in compaction on the cap surface. It should be noted that the intersection point of the Drucker-Prager and the elliptical yield surfaces is determined by solving the corresponding system of Equations ((8))-(11). Based on these equations, the movement of the intersection point depends on the intensity and type of plastic deformation of the material. During compaction, the intersection point and cap surface move to the right. While through the dilation, the movement is toward left. Moreover, to avoid non-uniqueness of the gradients at the intersection point, it is assumed that this point belongs to the elliptical yield surface.

Now, it can be seen that, in our model other than traditional parameters (c_0, α), we have additional parameters ($h, \gamma^*, n_1, n_2, m, r, \beta, \sigma'_0, \sigma'_1$) (see Table 1). These parameters are determined from standard rock tests under axial compression at different confining pressures. It is necessary to analyze loading diagrams constructed in different coordinates: axial load versus axial and transverse deformations. Consequently, it is possible to construct the dependences of pressure changes versus the variation of volumetric and shear plastic deformations.

In the region of shear and dilatancy, when ($\sigma' < \sigma'_0$), all parameters (h, γ^*, n_1, β) are calculated using standard stress-strain curves. This is a well-established procedure for the analysis of loading diagrams of standard experiments on the core samples. It is essential to build the initial yield surface corresponding to the elastic limit and the final one, which corresponds to the maximum strength, after which the failure begins. The evolution of the yield surface from the initial to the final state is described by the equations (5)–(7), as was proposed earlier.^{16,51} The parameters of the elliptical yield surface and its evolution are determined using the loading diagrams under hydrostatic and high confining compressions. The evolution of the elliptical part is described by the Equations (8)–(11), which are driven from analysis of the loading diagrams. The major difficulty is the determination of the parameters describing the variation of σ'_0 and dilatancy coefficient (β). This may require more experiments with accurate measurement of volume changes during the deformation process. However, this does not necessitate the development and application of special techniques.

TABLE 1 Required parameters for description of plastic deformation

Dilation region ($\sigma' \leq \sigma_0$)	Compaction region ($\sigma_0 < \sigma' \leq \sigma_1$)
c_0, α - parameters of initial yield surface (the cohesion and the friction coefficient for Drucker-Prager yield surface)	σ_0, σ_1 - parameters of cap surface (initial)
h, γ^* - hardening parameters	$\varepsilon^* \approx \phi^*, r, m$ - parameters of cap expansion (hardening)
n_1, β_0 - parameters of the plastic potential (dilatancy parameters)	n_2 - parameter of plastic potential for compaction

Determining the parameters σ_0, σ_1 requires additional experiments at high confining pressures.²⁶ It should be noted that the threshold effective mean pressure (σ'_0) depends on the volume change and β on σ'_0 and the current stress state.

3 | SYSTEM OF EQUATIONS AND PLASTIC DEFORMATION

In terms of the governing equations, we numerically solve a system of equations, including equations of motion and continuity:

$$\sigma_{ij,j} + \rho F_i = \rho \dot{u}_i \quad (14)$$

$$\dot{\rho} + \rho u_{i,j} = 0, \quad (15)$$

and substituting Equation (1) to Equation (14), we obtain the equation of motion as a function of effective stresses:

$$\dot{\sigma}'_{ij,j} - \alpha_B P_{p,j} + \rho F_i = \rho \dot{u}_i, \quad (16)$$

where ρ is the density of representative elements of the material; u_i are the velocity vector components; σ'_{ij} are the Cauchy effective stress tensor components; $\dot{\varepsilon}_{ij}$ are the Cauchy strain rate tensor components; and F_i are the mass forces. The dot above a variable denotes the Lagrange time derivative, and the subscript after a comma represents the corresponding coordinate derivative. In this work, the standard convention for the summation over repeated indices is employed.

The relation between stress and strain for the elastic behavior is described by the hypoelastic law:

$$\dot{\sigma}'_{ij} = -\sigma' \delta_{ij} + s_{ij}, \quad (17)$$

$$\dot{s}_{ij} = 2\mu \left(\dot{\varepsilon}_{ij}^e - \frac{1}{3} \dot{\varepsilon}_{kk}^e \delta_{ij} \right), \dot{s}_{ij} = \dot{s}_{ij} - s_{ik} \dot{\omega}_{jk} - s_{jk} \dot{\omega}_{ik}, \quad (18)$$

$$\dot{\varepsilon}_{ij} = \frac{1}{2} (u_{i,j} + u_{j,i}), \quad (19)$$

$$\dot{\omega}_{ij} = \frac{1}{2} (u_{i,j} - u_{j,i}), \quad (20)$$

$$\dot{\sigma} = -K \frac{\dot{V}}{V}, \quad (21)$$

where $\dot{\omega}_{ij}$ are the rotational velocity tensor components; δ_{ij} is the Kronecker delta; K and μ are the bulk and shear moduli, respectively. The stress tensor is decomposed into spherical (hydrostatic) σ' and deviatoric s_{ij} parts. For the strain rate tensor $\dot{\varepsilon}_{ij}$, it is assumed that

$$\dot{\varepsilon}_{ij} = \dot{\varepsilon}_{ij}^e + \dot{\varepsilon}_{ij}^p, \quad (22)$$

where $\dot{\varepsilon}_{ij}^e$ and $\dot{\varepsilon}_{ij}^p$ are the elastic and plastic parts of the strain rate tensor, respectively.

Deformation processes in the geological media are simulated through the use of an approach based on solving the system of dynamic equations for an elastoplastic medium by an explicit numerical finite-difference scheme.^{52,53} In order to consider quasi-static problems, the loading rate (load change) was very smoothly applied. It is quite essential to ensure such conditions are not only at the stage of development of plastic deformation and the formation of localization bands but also at all stages so that there are neither large oscillations of stress nor waves with large amplitudes. In this case, the dynamic effects in the form of the propagation of elastic waves and stress oscillations become negligible. In addition, artificial viscosity algorithms were used for oscillation damping associated with dynamic effects and ensuring the stability of the calculation and elimination of non-physical effects.⁵⁴ With the proper selection of artificial viscosity parameters, *it does not have a noticeable effect on the obtained solution, including the thickness of the localization bands.* Different variants of the computation technique with oscillation damping are used in many methods (both commercial and research), although this is not usually discussed in publications.^{55,56}

At the same time, very small stress fluctuations allow us to simulate the inception of deformation localization bands without a special introduction of artificial heterogeneities. At the stage of hardening of the medium, these fluctuations have no effect on the distribution of the stress-strain state. Their influence is many orders of magnitude lower than the effect of any heterogeneities and geometric irregularities, including the wellbore. However, in the homogeneous state zone after the completion of the hardening stage, the small oscillations of stresses lead to the formation of a multitude of strain localization nuclei. As the deformation develops, most of them stop developing, and some develop further. As a result, localization zones are formed. The critical point is that the development of irreversible strain localization bands is completely controlled by the constitutive relations and loading conditions. This is confirmed by many calculations, eg, Stefanov et al.¹⁶

The numerical model in this work is based on a modified 2D plane strain formulation orthogonal to the cross-section of the wellbore (see APPENDIX A for modification of the 2D plane strain). The plastic strain is computed by the yield surface and plastic potential equations:

$$f(\sigma'_{ij}, \varepsilon_{ij}^p) = 0, \quad (23)$$

$$g(\sigma'_{ij}, \varepsilon_{ij}^p) = 0, \quad (24)$$

$$d\varepsilon_{ij}^p = \lambda \frac{\partial g}{\partial \sigma'_{ij}}, \quad (25)$$

where f is the yield function, g is the plastic potential, ε_{ij}^p is the plastic strain component, and λ is a non-negative plastic flow-rate parameter, which is different by a change in position in a specific time and by a change in time in a specific position.

The medium follows the law of elasticity before reaching the yield surface. As the stress crosses the yield surface ($f > 0$), such a stress state is inadmissible, and it should be returned to the yield surface. This point in the stress space moves normal to the surface of the plastic potential until its intersection with the yield surface. This procedure follows on from the solution of the system of equations (eq. (17)–(25)). Therefore, the adjustment of stresses is carried out in order to satisfy the constitutive equations and conditions and also to compute the corresponding inelastic deformations.^{16,52}

4 | COMPUTATIONAL RESULTS AND DISCUSSION

Prior to studying the deformation processes around the wellbore, we investigated the deformation process of the rock sample under similar conditions in the laboratory. The aforementioned proposed mathematical model was applied to the Bleurswiller sandstone with dimensions of 3×6 cm. Bleurswiller is a high-porosity (25%) sandstone composed of 50% quartz, 30% feldspar, and 20% mica and oxides.^{10,57} Reproducing experimental observations allows us to improve

the precision of the achieved rock parameters and also validate the proposed numerical model for further wellbore stability analysis. As mentioned before, all rock parameters can be estimated through the standard triaxial test. The constitutive input parameters and rock physical properties used in the elastoplastic analysis for this rock were obtained as shown in Table 2 and 3.

For the simulation of the deformation process of rock specimens, similar to laboratory conditions, the rock sample was hydrostatically loaded in all directions until reaching the specified confining pressure (σ_c). Then by fixing confining pressure on lateral boundaries, the top side of the specimen was subjected to a given constant displacement rate (v_y), which led to an increment in axial stress and plastic deformation (see Figure 2a).

As previously noted, in order to avoid large oscillations in the loading process, the displacement rate of the upper boundary was smoothly changed from zero to given value $v_0 = 0.005 \text{ m/sec}$ linearly as $v_y(t) = v_0 t/t^*$ for $t < t^*$ and $v_y(t) = v_0$ for $t \geq t^*$. The time t^* of increasing the displacement rate was chosen so that the effect of oscillations associated with the dynamic formulation of the problem was negligible. For a given geometry, it is viable if $t^* \geq nD/V_p$ and

TABLE 2 Input parameters of the constitutive model

σ'_0 (MPa)	σ'_1 (MPa)	γ^* (%)	ε^* (%)	h	r	m	n_1	n_2
40	110	1.1	25	0.6	1.2	1.5	2	1.5

TABLE 3 Fluid and rock physical properties

Parameter	Value
Density (ρ , kg/m ³)	2250
Bulk modulus (K, GPa)	7.6
Shear modulus (μ , GPa)	2.7
Cohesion (c_0 , MPa)	5.8
Internal friction angle coefficient (α)	0.5
Initial dilatancy coefficient (β_0)	0.4
Biot's coefficient (α_B)	1.0
Hydraulic diffusivity ($k/\mu\phi c_r$, m ² /sec)	5e-5

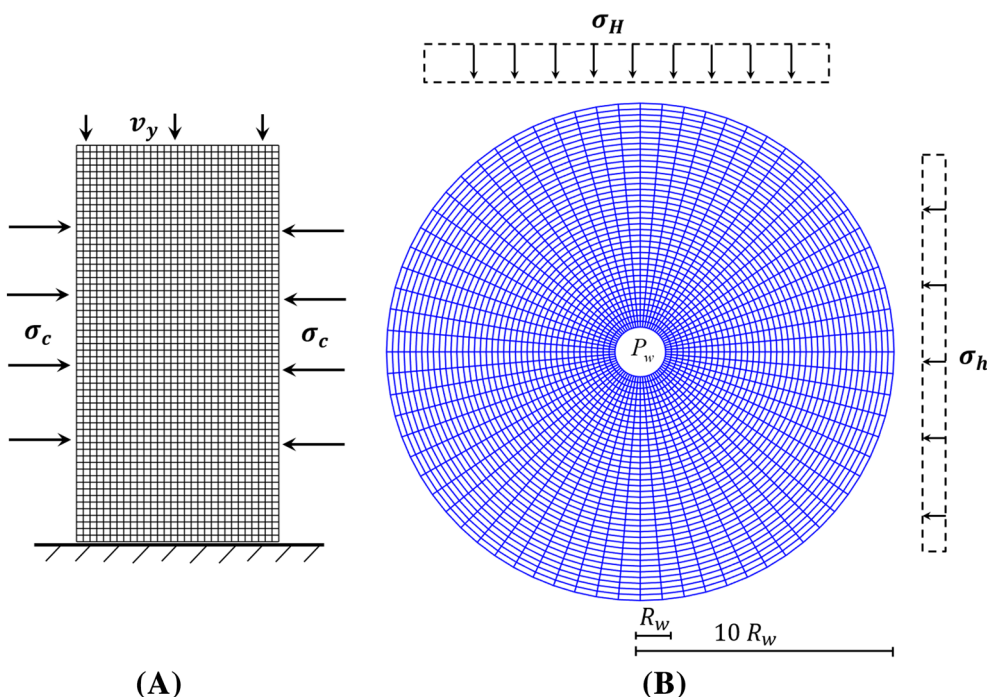


FIGURE 2 (a) Scheme of specimen loading and (b) computational domain for wellbore stability analysis including far-field stresses and mud pressure within the hole

$n > 20$, where D is the maximum dimension of the investigated object and V_p is the wave propagation speed in the medium.⁵⁵

Figures 3–5 show the numerical scheme verification and results of deformation processes on this sandstone for both brittle and ductile behaviors. Simulation results of shear damage and grain crushing that lead to the formation of localized bands show to be consistent with experimental observations.^{10,58,59} Depending on the confining pressure level, the rock exhibits shear or compaction localized bands. In a low confining pressure level ($\sigma_c = 20$ MPa), deformation is localized onto a single discrete shear fracture plane (Figure 4a). In high confining pressures ($\sigma_c = 80, 100$ MPa), deformation is localized into several compaction bands and the dominant micromechanical damage processes are grain crushing and pore collapse.^{10,60} These bands are oriented slightly oblique, and, with increasing the confining pressure, they are going to be perpendicular to the maximum principal stress (Figure 4b,c). In the above cases, the localization of deformation occurs at different values of the axial deformation. To put it another way, the initiation of the softening process triggers the localization of deformation, and, during the hardening, no localization takes place. Its inception depends on the deformation mode (dilatancy or compaction) and the level of confining pressure. On Figure 3a, the pressure and volumetric strain values are marked by red stars when the localization process begins.

Simulation of rock behavior under hydrostatic compression shows uniform compaction of the specimen without any localized bands (Figure 5a). The difference in inelastic volumetric strain is about $4e-3$ percent on the edge of the sample. Figure 5c shows the evolution of compaction bands at the sequential moments of time under $\sigma_c = 100$ MPa. Under constant applied strain rate, the compaction bands propagate with time until most of compaction bands cover the core completely.⁵⁹ Recent experimental and numerical studies on Bleurswiler sandstone also show the tendency of this rock to develop the compaction bands under creep condition.^{59,61,62}

The problem of mesh-dependency is characteristic of numerical solutions related to plastic deformation in an inhomogeneous medium, as well as localization of deformation and failure. This is due to the non-uniform distribution of stresses, stress concentration, and the presence of a stress gradient. Accordingly, the satisfaction of the criteria of plasticity and failure, as well as the magnitude of the irreversible deformation, depends on the step of the spatial coordinate and, hence, the step of the grid. To reduce the influence of mesh size usually regularization methods, gradient models, nonlocal criteria, and strong discontinuity formulations are used.^{32,63}

FIGURE 3 Effective mean stress versus volumetric strain (porosity reduction) at different confining pressures (σ_c): (a) numerical simulation results and (b) sample deformation measured through laboratory experiments (after Fortin et al¹⁰)

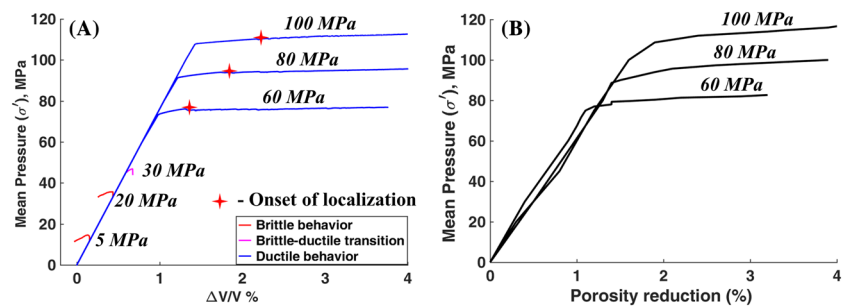
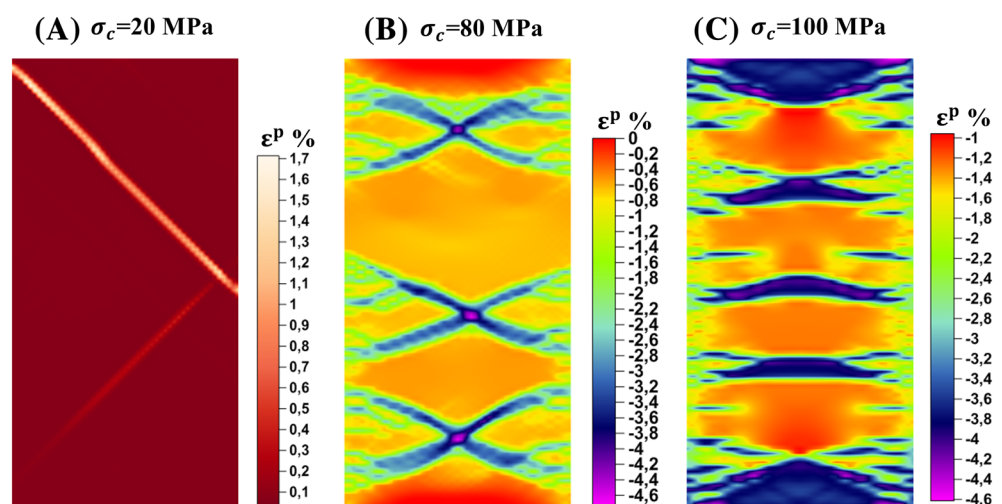


FIGURE 4 Results of numerical simulation of rock behavior (strain localization) at different confining pressures (σ_c): (a) intensity of inelastic volumetric strain of deformed sample in shear-induced dilation regime ($\sigma_c = 20$ MPa) and (b-c) in shear-enhanced compaction regime ($\sigma_c = 80, 100$ MPa)



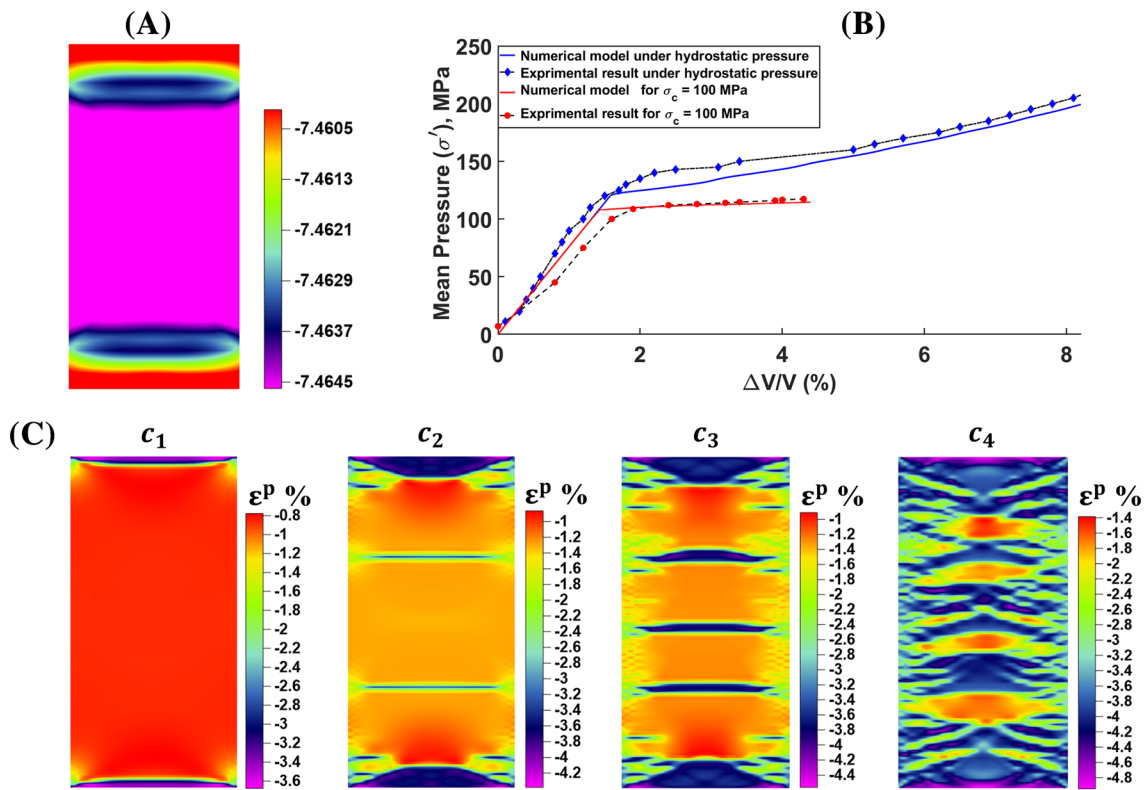


FIGURE 5 (a) Uniform compaction of the specimen under hydrostatic compression, (b) numerical and experimental response of volumetric strain versus effective mean stress, and (c) the evolution of compaction bands at sequential moments of time under $\sigma_c = 100$ MPa

The introduction of a spatial scale, the transition to nonlocal models, can significantly reduce the influence of the grid spacing. The simplest way to reduce the influence of the mesh is to take the mesh size into the plasticity criterion, similar to introducing the factor \sqrt{x} in the failure criterion for crack growth.⁵² In this case, in fact, the material becomes stronger or weaker proportional to the scale-factor. However, the dependence of the localization bandwidth, and, accordingly, the plastic deformation in it on the grid size will remain.

The presence of different types of features and their singularity greatly complicates the solution of this problem. During modeling, various mechanisms of irreversible deformation may develop, depending on the specific problem and mathematical model. The jump in deformation in the case of the shear band is not limited, but the jump in the volumetric deformation in the compaction bands cannot be large because compaction develops with an increase in the stresses. With increasing load, the compaction bands expand. Thus, it becomes extremely difficult to eliminate the influence of the grid size, taking into account all the features, and a significant complication of the model is necessary.

Through solving any problem, there is always a question of a compromise between the required accuracy of the solution, the complexity of the solution, and the availability of the necessary data. Considering the process of deformation around the borehole, we have a host of uncertainties about the loading conditions and rock properties, as well as many different interrelated processes that have different degrees of influence on the near-wellbore zone. Undoubtedly, this does not reduce the requirements of description accuracy in processes that are being studied. Taking into account the localization, a very salient point in modeling the deformation process is the load increment step. The largest errors can occur if the increment is too large because both the process of deformation development in the localization zone and the change in the stress state around it depend on this. Intrinsically, this process proceeds in time, and it is necessary to consider the entire sequence of state changes.

In this study, no special procedures are used to eliminate the dependence on the grid size. However, to describe the deformation process, we solve a system of dynamic equations. A small increment of the loads provides good accuracy in the description of the process of plastic deformation, as well as a minor influence of dynamic effects. This enables us to consider the process as quasi-static without analyzing the dynamics of wave processes because they are very small. However, the influence of mesh size is present. A change in the grid spacing leads to a refinement of the location, number, and length of different types of localization bands. Implementation of a dynamic approach explicitly to simulate strain localization of quasi-static problems using the elastoplastic models to some extent overcomes the non-uniqueness

issue.^{64,65} This is related to the fact that, in such an approach, the deformation process, including localization, evolves in time.

Figures 6 and 7 show that the location and form of the localization bands do not depend on the mesh size and the smaller mesh size causes the more detailed depiction of the deformation development.

The significant complication in the formulation of problems and methods of solution leads to the fact that, in practice, one prefers to use strongly simplified formulation (analytical models based on the elastic solution), which leads to significant errors. Therefore, our aim was to find a compromised solution that can help solve difficult practical

FIGURE 6 Simulation results of inelastic volumetric strain variation (localization pattern) in the specimen with (a) 15×30 and (b) 25×50 and 50×100 computational domain grid

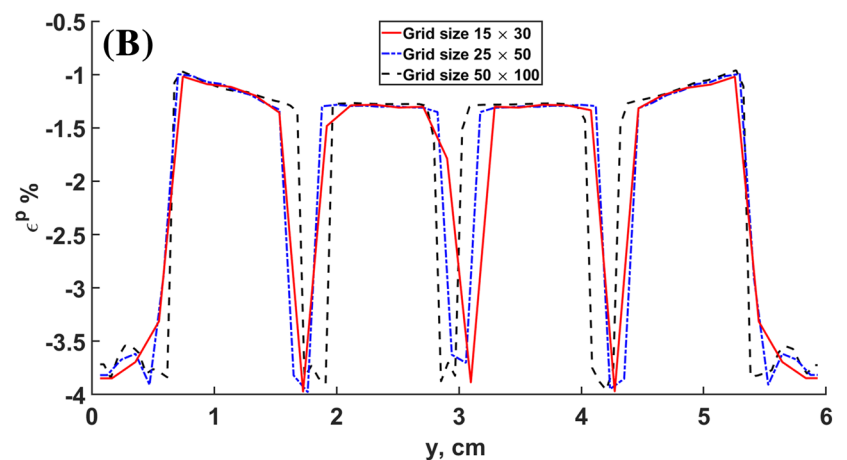
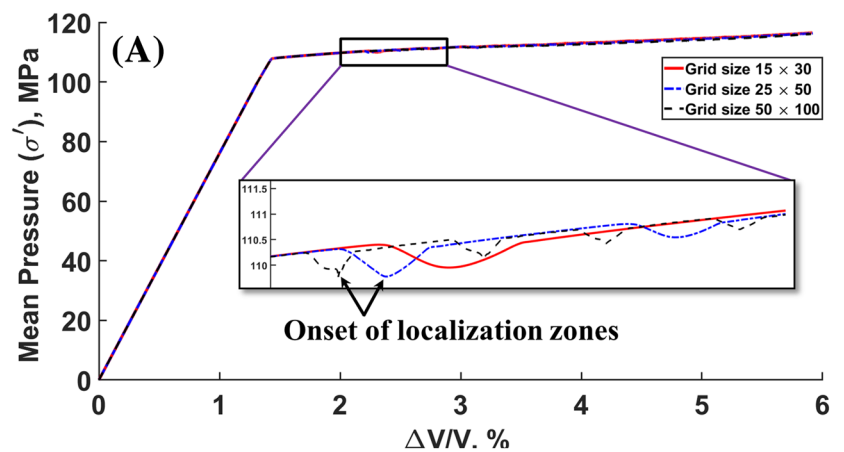
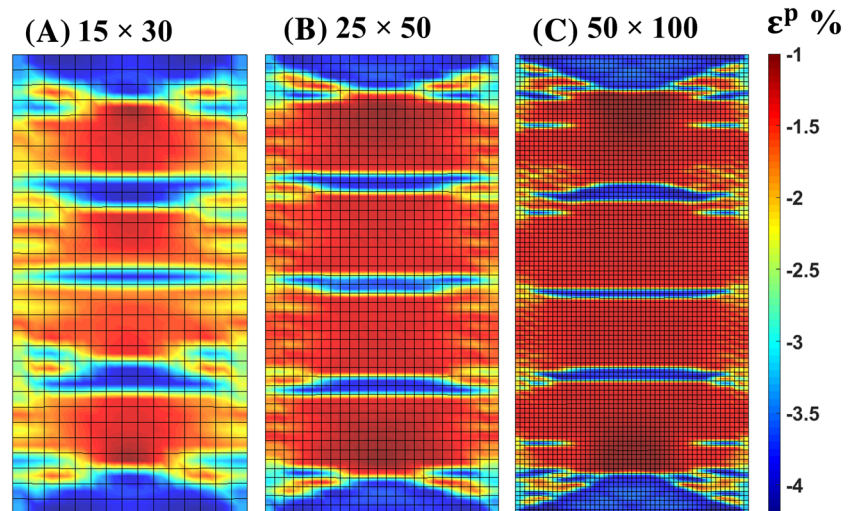


FIGURE 7 (a) Effective mean stress versus volumetric strain and (b) inelastic volumetric strain variation along the y -axis through the center of the specimen for different mesh sizes

problems without significantly complicating them and show specific features of the development of irreversible deformation around the wellbore after drilling.

The main goal of our work is to demonstrate the possibility of developing different types of inelastic deformation localization, which affect the stability and the filtration properties alteration in the near-wellbore zone. The concentration of stress in the near-wellbore zone generated due to drilling has the greatest impact on the nature of the development of deformation, type, and length of localization bands. Depending on the stress state, localized shear bands and compaction bands may develop around the wellbore.

The behavior of the studied Bleurswiller sandstone for wellbore stability analysis under different reservoir conditions is investigated using the proposed model. It was assumed that the medium is homogenous and the reservoir is infinite-acting, ie, a reservoir with no apparent outer boundary limit affecting fluid flow during a short period.

The boundary loading for wellbore stability analysis also consists of two stages: first, the vertical and horizontal stresses are applied in undisturbed conditions, in order to simulate the initial in-situ stress state before the drilling process (see Figure A1). Taking into account the modified plane strain condition and dividing the total stress into volumetric or mean (σ) and deviatoric (s_x, s_y, s_z) stresses, the initial stress state can be stated as follows:

$$\begin{aligned}\sigma^0 &= -\left(\frac{\sigma_{xx} + \sigma_{yy} + \sigma_{zz}}{3}\right), \\ s_{xx}^0 &= \sigma_{xx} + \sigma^0, \\ s_{yy}^0 &= \sigma_{yy} + \sigma^0, \\ s_{zz}^0 &= \sigma_{zz} + \sigma^0.\end{aligned}\quad (26)$$

Subsequently, the stresses in the elements corresponding to the borehole (at $r = R_w$) during drilling time ($0 < t \leq t^*$) are very smoothly changed with time to simulate the process of drilling as follows:

$$\begin{aligned}\sigma^b &= \sigma^0 \left(1 - \frac{t}{t^*}\right) + P_w \left(\frac{t}{t^*}\right), \\ s_{xx}^b &= s_{xx}^0 \left(1 - \frac{t}{t^*}\right), \\ s_{yy}^b &= s_{yy}^0 \left(1 - \frac{t}{t^*}\right), \\ s_{zz}^b &= s_{zz}^0 \left(1 - \frac{t}{t^*}\right),\end{aligned}\quad (27)$$

which finally at $t = t^*$ approach the boundary conditions as

$$\begin{aligned}\sigma^b &= P_w, \\ s_{xx}^b &= s_{yy}^b = s_{zz}^b = 0.\end{aligned}\quad (28)$$

In such a way, the physical time (t) when considering the dynamic processes of wave propagation becomes an internal parameter of the computation, and t^* is the time during which a quasi-stationary state is established. Considering quasi-stationary processes, when the state of the medium changes under the influence of a gradual change in the load (for example, pressure in the borehole), the parameter t^* is taken as a unit of time. This parameter is used to coordinate the rate of load change, including pore pressure, as well as rheological and kinetic parameters if they are taken into account.

The domain size considered for the numerical simulation is ten times the radius of the wellbore, and the complete geometry with the prescribed boundary conditions is provided in Figure 2b. This domain size would be sufficient to ensure the absence of the external boundaries' influence on the development of the process in the studied zone. The wellbore stability analysis was carried out for different wellbore conditions in a borehole with a 0.25 meters radius. During the drilling, the effect of over- and under-balanced pressures ($P_w > P_p$ and $P_w < P_p$) on the formation of plastic deformation zone and alteration of effective stresses around the wellbore were also investigated. The numerical model was validated based on the elastic solution for effective stress around the borehole. The difference between the result of

the numerical model and the analytical elastic solution proved to be less than 0.01%.⁶ Considering elastoplastic deformation in the process of numerical modeling, once elements next to the wellbore reach to the end of the softening process period, they are removed from the mesh system, and the wellbore boundary condition is updated on the newly exposed faces. A parametric study has been done to study the effect of different parameters under different conditions on stability analysis. The sign of stresses has been multiplied by a minus sign in all figures for ease of understanding to readers. We assumed that the pore pressure relaxation time is shorter than the inelastic deformation process. This means that the deformation process develops slowly enough and the pore pressure does not change and preserves its distribution at each time step around the wellbore. It is important to notice that the pressure distribution Equation (2) is valid only when the wellbore maintains its integrity in the form of a circle without severe breakouts. Therefore, the pressure distribution was included only in Section 4.1, where the wellbore retains its shape (no breakouts). Therefore, in this section, we have an additional stage of loading variation corresponding to the state of the near-wellbore zone after 1 h of underbalanced drilling (for this case, three stages). At this stage, the influence of changes in the distribution of pore pressure over a certain time was considered. The pore pressure distribution around the wellbore after 1 h (P_p^{1h}) with fixed wellbore pressure (P_w) using Equation (2) is calculated. Similar to Equation (27) for load changes at the wellbore boundary, in this stage, the pore pressure distribution in the equation of motion (eq. (16)) is gradually changed until at $t=t^{1*}$ approaches to the desired state as follow:

$$P_p = P_0 \left(1 - \frac{t}{t^{1*}}\right) + P_p^{1h} \left(\frac{t}{t^{1*}}\right). \quad (29)$$

The change in pore pressure was also carried out gradually so that the state of the medium remained quasi-stationary. The values of t^* and t^{1*} are estimated similar to the experimental simulation so that, when the load becomes constant, the stress state of the medium ceases to change. The parameter D for wellbore analysis was assumed to be equal to the maximum dimension of the investigated object, ie, ten times the diameter of the borehole. The pore pressure and wellbore pressure in Sections 4.2 and 4.3 were assumed to be equal, in order to exclude pressure diffusion around the wellbore.

4.1 | Effect of wellbore pressure during drilling

The well was analyzed for stability under different wellbore pressure (drilling fluid density) values. Reservoir pressure, depth, and the initial stress state determine the required density of the drilling system. Both overbalanced (OB; when $P_w > P_p$) and underbalanced (UB; when $P_w < P_p$) drilling conditions were applied to investigate the variation of the effective stresses and the inelastic zone around the wellbore (case 1). The deformation characteristics around the wellbore are defined as the ratio of the effective stresses to the mechanical properties of the rock. Figure 8a shows the effective stress distribution with 2 MPa OB pressure in the direction of minimum horizontal stress for elastoplastic and elastic models. Here, the direction of minimum horizontal stress was assumed to be in the x-direction. The graph confirms that the tangential stress is considerably lower in the elastoplastic case as a result of plastic deformation as compared with the elastic case.

Under the given conditions and parameters of the model, the size of the plastic zone was at most 30% of the size of the wellbore radius. It was assumed that, during OB drilling and formation of the filter cake, no pressure connection between wellbore and reservoir is present. Therefore, no change is observed in the effective stress during OB drilling. Numerical experiments reveal that the plastic zone in the OB drilling is smaller than that of the UB drilling (zone A in Figure 8b). During underbalanced drilling, the hydrostatic head of drilling fluid is designed to be less than reservoir pressure, this implies that there is a continuous flow of hydrocarbon into the well and pore pressure reduction with time around the wellbore with the consequent rise in the effective stress is observed. As shown in Figure 8b, there is a wider plastic zone in the vicinity of wellbore under 2 MPa UB pressure as compared with 2 MPa OB pressure (Zone B). Figure 8 also shows that in the 2 MPa UB pressure, a slight change in effective stresses does not have a significant effect on the size of the plastic zone. Figure 9 represents stress and strain distributions around the borehole for 2 MPa OB pressure. As observed, the greatest values of the tangential shear stresses are located at a small distance from the wellbore wall (the boundary of the plastic zone).

Figure 10 represents the distribution of the strength parameter (left), an indicator of wellbore stability, that changes with hardening or softening processes and also the accumulated inelastic equivalent shear strain (right). Under 2 MPa

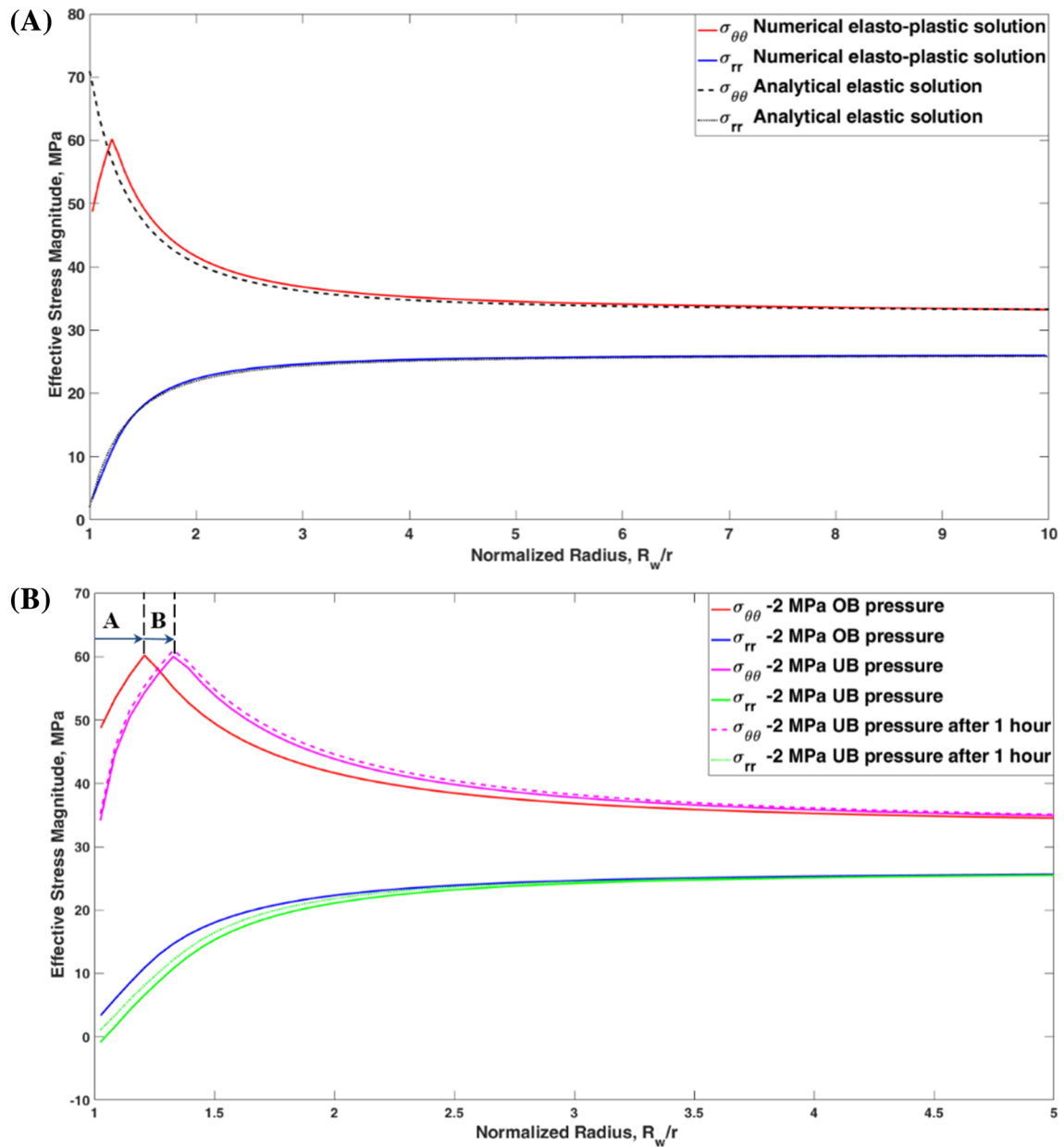


FIGURE 8 (a) Effective stress distribution in elasto-plastic model versus elastic model in the direction of minimum horizontal stress (b) plastic zone and effective stress variation in OB and UB drilling

OB pressure, the maximum accumulated inelastic equivalent shear strain is about 1%, which is less than the critical value γ^* (Figure 10a, right). This translates into the strength hardening process and stable condition around the borehole (Figure 10a, left). During the UB drilling regime, the maximum accumulated inelastic equivalent shear strain is about 1.5%, which indicates the beginning of material degradation around the borehole in the direction of minimum horizontal stress (Figure 10b, right). The white dotted lines on the left side of Figure 10b indicate zones in which the rock softening process begins.

4.2 | Effect of in situ stress anisotropy

Zoback et al⁶⁶ and Vernik et al⁶⁷ presented detailed measurements of the cross-sectional shape of breakouts by using specially processed data from an ultrasonic wellbore televiewer and developed the theoretical analysis of the

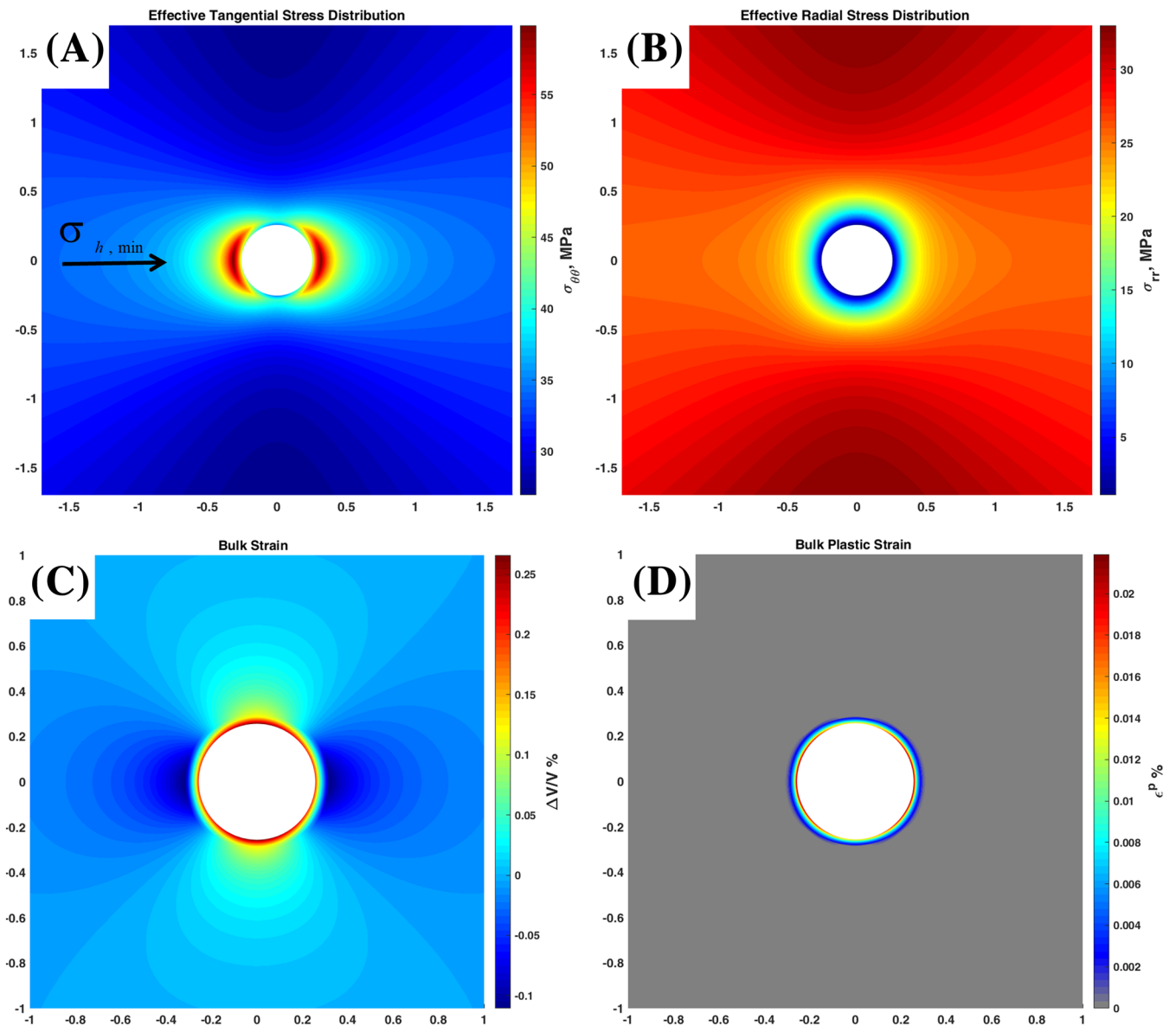


FIGURE 9 State of stress and strain around the borehole with 2 MPa OB pressure, (a) effective tangential stress, (b) effective radial stress, (c) volumetric strain (both plastic and elastic), and (d) accumulated inelastic equivalent shear strain, ($\sigma_V/\sigma_H/\sigma_h/P_w = 68/61/54/30$ MPa)

mechanism of formation breakout. Haimson⁶⁸ also investigated the different borehole breakout failure micromechanisms that observed in the laboratory under optical and scanning electron microscopes.

In this section, the shape of the plastic zone was studied under different in situ stress anisotropy (Table 4, case 2). It was assumed that the drilling pressure in the wellbore was the same as pore pressure and minimum horizontal stress is decreased from 61 to 41 MPa. The mesh size is selected sufficiently small to consider detailed plastic deformation. Localization bands actively develop as soon as the accumulated shear strain reaches a critical value γ^* and, accordingly, the value of cohesion begins to decrease (Figure 11a).

Under the isotropic condition, far-field stresses are not sufficient to initiate breakouts and the stress and plastic strain are uniformly distributed around the borehole. The transition from isotropic to anisotropic is accompanied by an increase in the deviatoric part of the effective stress tensor, which leads to the development of plastic deformation, rock degradation, localized shear zones formation, and, finally, rock failure. At far-field stresses anisotropy above a critical level, rock pieces between conjugate shear cracks spall off on opposite sides of the borehole aligned with the minimum horizontal stress (Figure 11). The simulated breakouts have the same dog-ear shape as laboratory results obtained by

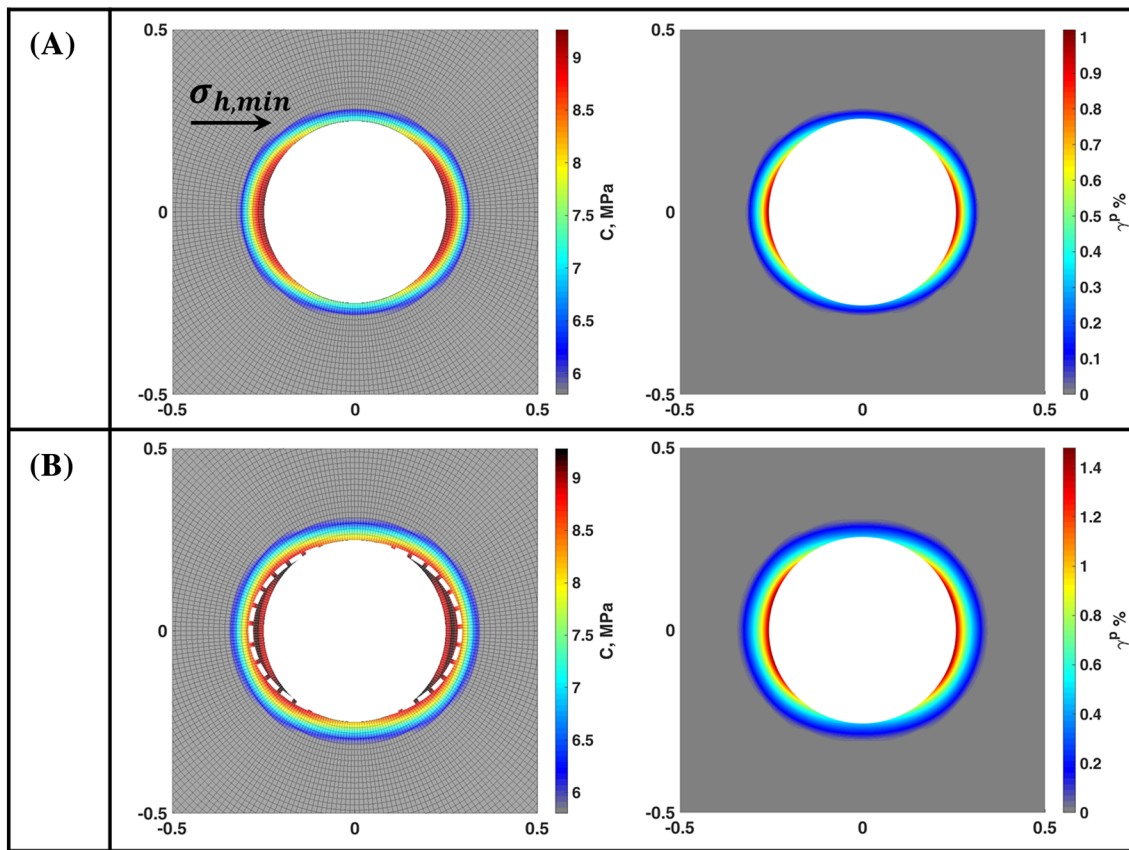


FIGURE 10 State of cohesion with considering the hardening and softening of material (left) and the accumulated inelastic equivalent shear strain (right) under different drilling regimes, (a) 2 MPa OB pressure and (b) 2 MPa UB pressure (the white dotted lines indicate zones in which the rock softening begins)

TABLE 4 Input parameters for wellbore stability analysis under different conditions

	P_w	P_p	σ_v	σ_H	σ_h
Case 1	26, 30	28	68	61	54
Case 2	28	28	68	61	61, 54, 46, 41

Haimson.⁶⁸ The most remarkable outcome of the numerical analysis is the calculation of stress concentration at the tip of breakouts (Fig. 11d, e, and f).

An increase in effective stresses at the tip of breakouts can lead to a change in the mechanism of irreversible (plastic) deformation from the dilatant to the compactant, in which crushing and repacking of the grains occur. The high compressive stress concentration along the dog-eared breakouts appears to induce a compaction zone. Accordingly, we can explain the occurrence of grain crushing and porosity reduction at the breakout tip, which were observed experimentally by Haimson.⁶⁸ Negative inelastic volumetric strain in Figure 11c indicates the compressional deformation along the tips, and this phenomenon is referred to shear-enhanced compaction. Elongation and width of the compaction localization zone depend on the stress state and physical properties of the rock.⁶⁸ These numerical experiments serve as complementary proofs for the mechanism of shear breakouts and compaction localization development around the wellbore.

The plastic zone has a circular shape under isotropic in-situ stresses, and the accumulated inelastic equivalent shear strain is less than the critical value ($\gamma^* = 1.1\%$) at which the degradation of the material is initiated (Figure 12a). As the minimum horizontal stress decreases to 54 MPa, the plastic zone acquires an elliptical shape, and the maximum accumulated inelastic equivalent shear strain approaches its threshold value (Figure 12b). Decreasing the value of minimum horizontal stress to 46 MPa causes stress concentration in the direction of the minimum horizontal stress and the consequent formation of discrete plastic zones, which is in contradiction with the assumption of many semi-analytical

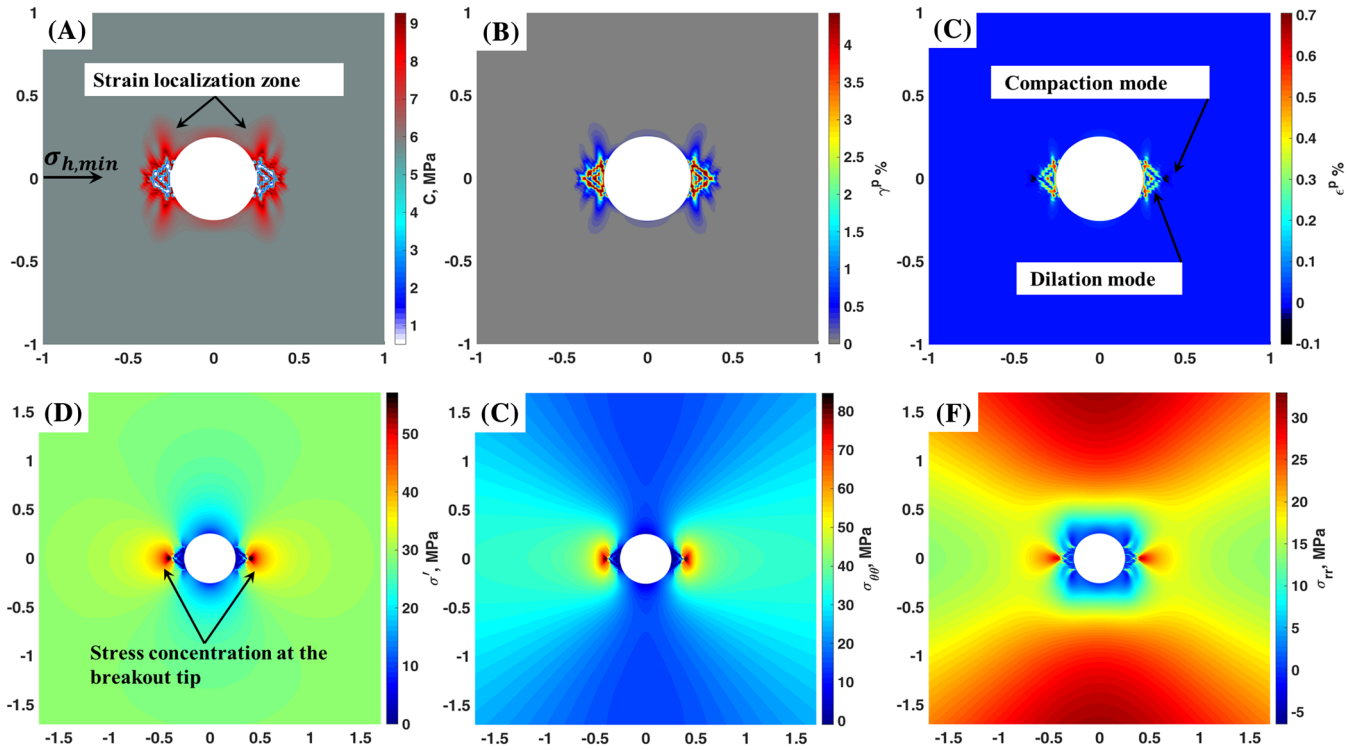


FIGURE 11 State of stress and plastic zone around borehole with high anisotropy in stress state, (a) cohesion variation, (b) accumulated inelastic equivalent shear strain, (c) inelastic volumetric strain, (d) effective mean pressure, (e) effective tangential stress, and (f) effective radial stress distribution, ($\sigma_V/\sigma_H/\sigma_h = 68/61/41$ MPa)

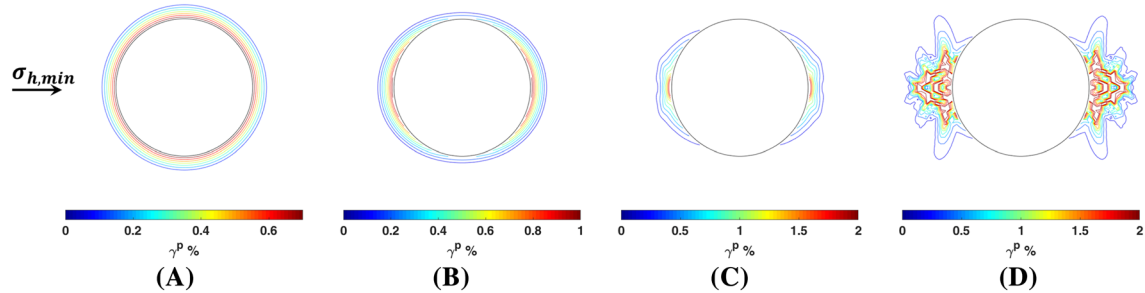


FIGURE 12 Schematic of plastic zone shape under different stress anisotropies ($\sigma_V/\sigma_H = 68/61$ MPa), (a) isotropic state ($\sigma_h = 61$ MPa), (b) $\sigma_h = 54$ MPa, (c) $\sigma_h = 46$ MPa, and (d) $\sigma_h = 41$ MPa

elastoplastic models^{19,22} (Figure 12c). At this step, the degradation (softening) of the medium is started. As the minimum horizontal stress decreases to 41 MPa, the shear failure along minimum horizontal stress occurs (Figure 12d). The numerical analysis illuminates that with the increase in stress differences across the plane, the plastic zone becomes narrower and deeper and the failure causes the plastic zone to take an irregular form. Spiezia et al⁶⁹ also investigated the influence of small imperfection on the inception and shape of localized deformation bands around the borehole.

4.3 | Effect of stress state on compaction localization

In order to exclude the effect of pore pressure distribution near the borehole on the intensity of plastic deformation and its shape, both pore and wellbore pressures were assumed to be equal to 28 MPa. This assumption allows for investigating the plastic deformation zone and local stress paths solely based on the mechanical properties of rock. The shape of the compaction localization zone just like the dilation regime strongly depends on geodynamical stress state, rock properties, and local stress paths. The intensity of compaction, failure width, and depth strongly depends on the elastic and

plastic parameters of rock. Different configurations of the regional stress state can lead to the formation of different localization patterns in the vicinity of the wellbore.

In the case of isotropic stress state, the irreversible deformation in the initial stage appears in the form of a circular zone that is uniformly distributed around the borehole. As mentioned before, small oscillations in the hardening stage do not affect the stress-strain state. Therefore, the plastic zone in case of no softening will keep its circular shape (Figure 13). Incorporating the softening process in the computation leads to the formation of spiral or radial localized bands, which usually intersect each other that consequently causes the formation of breakouts (Figure 14). In this case, there is no significant difference between the shape of the failure zones under compaction and those of the dilatancy regime. The main difference can be due to the slope of these bands, as well as the change in porosity. Under compaction mode, the localization bands have an inclination angle greater than 45 degrees to the direction of maximum compressive stress.

At the same time, the nucleation and development of localization bands in the shear-dilatancy and shear-compaction modes are somewhat different. In the first case, the development of localization bands occurs when there is some heterogeneity and when the accumulated plastic deformation exceeds the limiting value, γ^* and the strength decreases, as noted in Figure 11. In the second case, the development of the shear-compaction bands can begin for the same reason, as well as if the rate of expansion of the Cap surface as a result of compaction and reduction of porosity is not too high. This is usually observed in highly porous rocks. The influence of the different parameters, including the expansion rate of the Cap surface, is shown in the work of Stefanov et al.¹⁶

As noted above, under conditions of no stress concentration caused by heterogeneities or geometry, multiple nucleations of localization zones occur. This is due to the presence of small stress oscillations since the system of dynamic

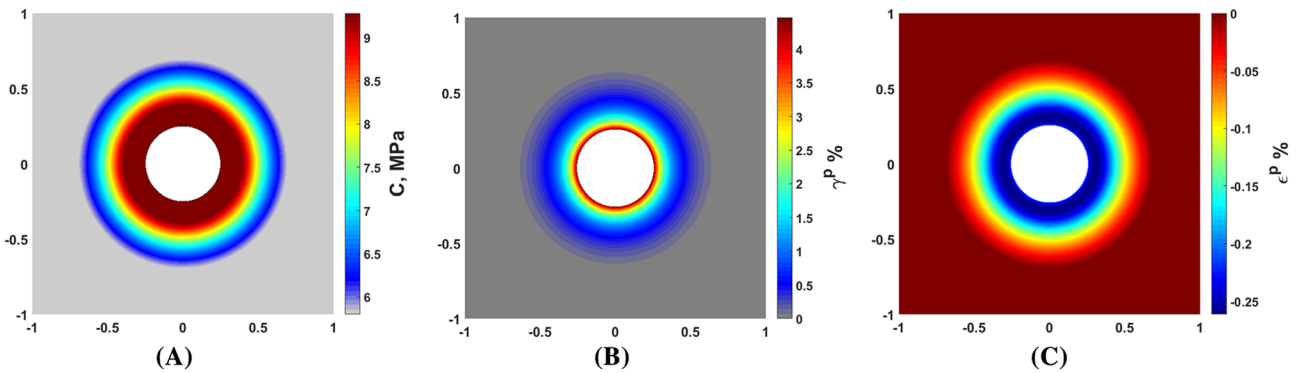


FIGURE 13 Drilled borehole under uniform principal horizontal far-field stresses without softening, (a) cohesion variation, (b) accumulated inelastic equivalent shear strain, and (c) inelastic volumetric strain, ($\sigma_V/\sigma_H/\sigma_h = 120/90/90$ MPa)

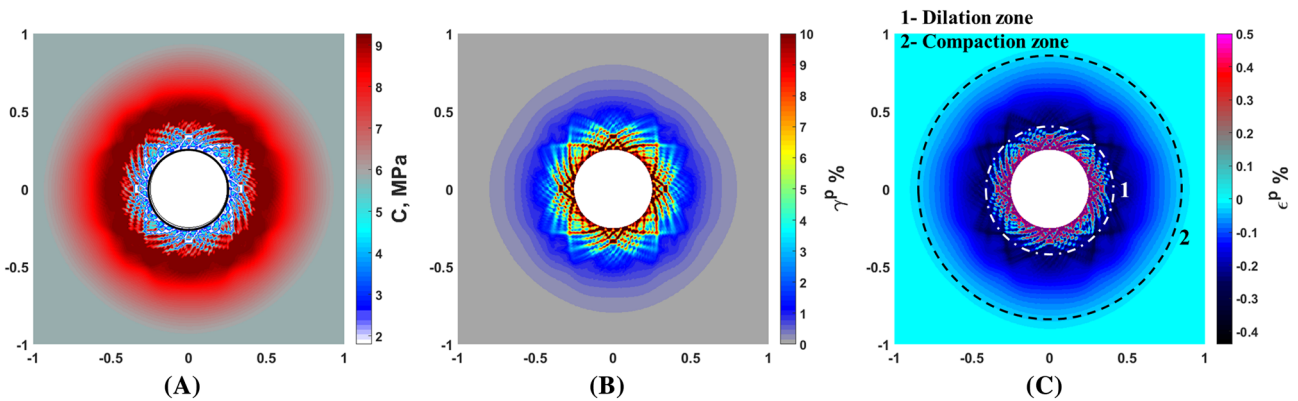


FIGURE 14 Formation of shear-dilation and shear-compaction localization zones around the wellbore under similar conditions as Figure 10 along with softening process, (a) cohesion variation, (b) accumulated inelastic equivalent shear strain, and (c) inelastic volumetric strain

equations is solved. Subsequently, as they grow, only parts of the bands develop, and the stress state becomes non-uniform. This leads to the appearance of the concentration regions associated with these localization zones. The nature of the development of localization bands is determined by the stress state and the defining parameters of the constitutive model. Thus, applying such approach for calculations, there is no need to artificially add heterogeneities that would lead to non-uniformities of the stress state.

In the case of anisotropic stress state, the basic deformation develops along the minimum horizontal stress that is similar to the case of dilatancy regime. In this case, the region of the generation of localization bands is exclusively determined by the loading conditions. The plastic deformation area takes a needle-shaped (Figure 15) or butterfly-shaped (Figure 17) depending on the initial stress state and local stress paths of the near-wellbore zone. In these cases, the localization zone often takes the form of bands passing through the center of the plastic zone. The plastic region in the form of a butterfly is the characteristic shape for the dilatancy regime, but there is a noticeable difference in these cases. Under the dilatancy regime, the butterfly's wings are more widely extended in the direction of the most compressive stress with an approximate slope of about 45 degrees (Figure 19a). However, under the compaction regime, the wings are extended in the direction of the least compressive stress, as in Figures 15 and 19b. The localization zones are developed at an angle from 45° to 90° with respect to the maximum principal stress depending on the initial stress state, physical properties of the medium, and local stress paths.^{36,70} Figure 19 shows various configurations of possible plastic

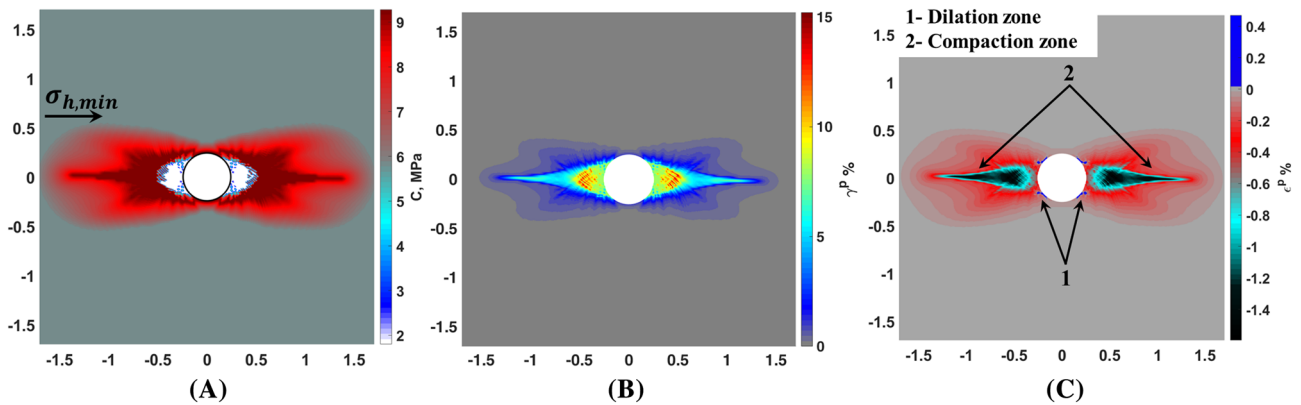


FIGURE 15 Formation of long and narrow (needle-shaped) compaction band ahead of breakout, (a) cohesion variation, (b) accumulated inelastic equivalent shear strain, and (c) inelastic volumetric strain, ($\sigma_V/\sigma_H/\sigma_h = 85/110/95$ MPa)

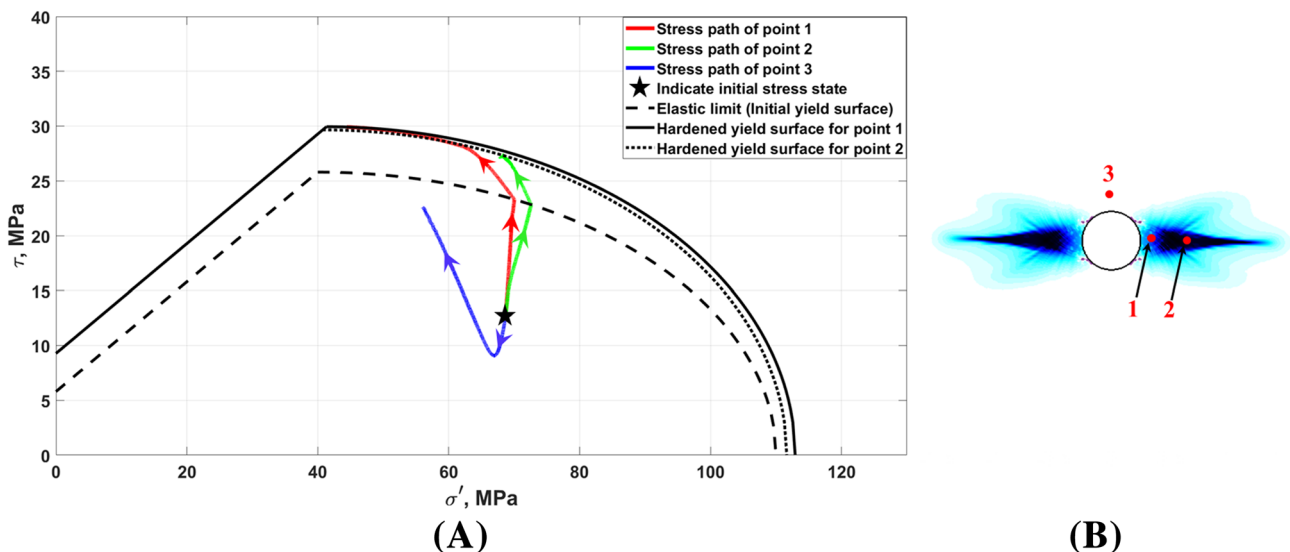


FIGURE 16 (a) Stress paths of the selected points and the corresponding yield surfaces and (b) configuration of the plastic zone and the position of investigated points

zones in compaction mode, which are not observed in the dilatancy regime. A localization region with a needle-shaped (Figure 15) has a more pronounced nature that is not observed in the dilatancy regime. This type of localization is similar to Haimson's⁶⁸ experimental observations in St. Peter sandstone, in which a long and narrow band of shattered and crushed grains was extended ahead of the breakout.

It should be noted that the development of irreversible deformation in the vicinity of the high-porosity wellbore rarely occurs strictly in compaction mode. Most often, it is possible to see also the dilatancy zones, which are formed in a thin layer around the wellbore, as well as along the edges of the compaction zone.⁷¹ This is not always easy to see in

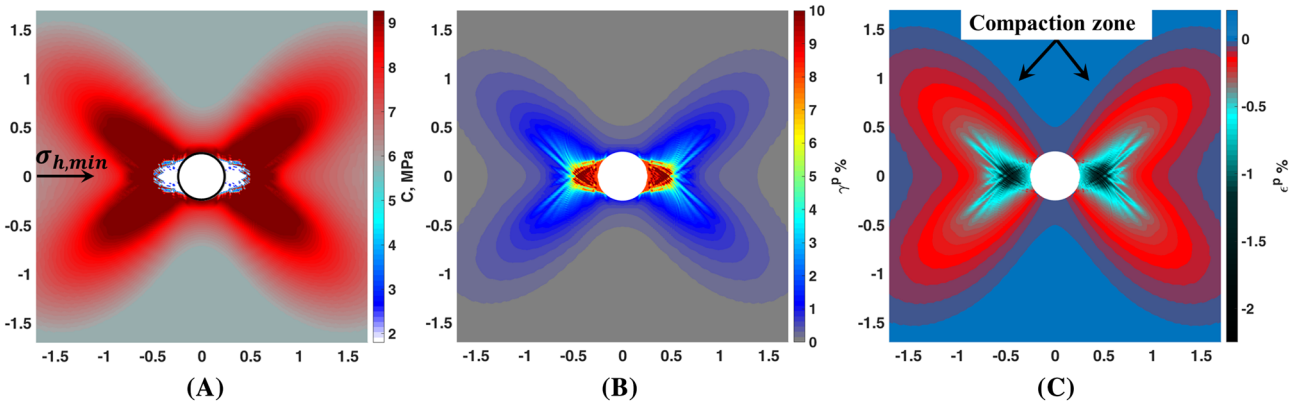


FIGURE 17 Formation of butterfly-shaped compaction localization zone around the borehole, (a) cohesion variation, (b) accumulated inelastic equivalent shear strain, and (c) inelastic volumetric strain, ($\sigma_V/\sigma_H/\sigma_h = 120/110/80$ MPa)

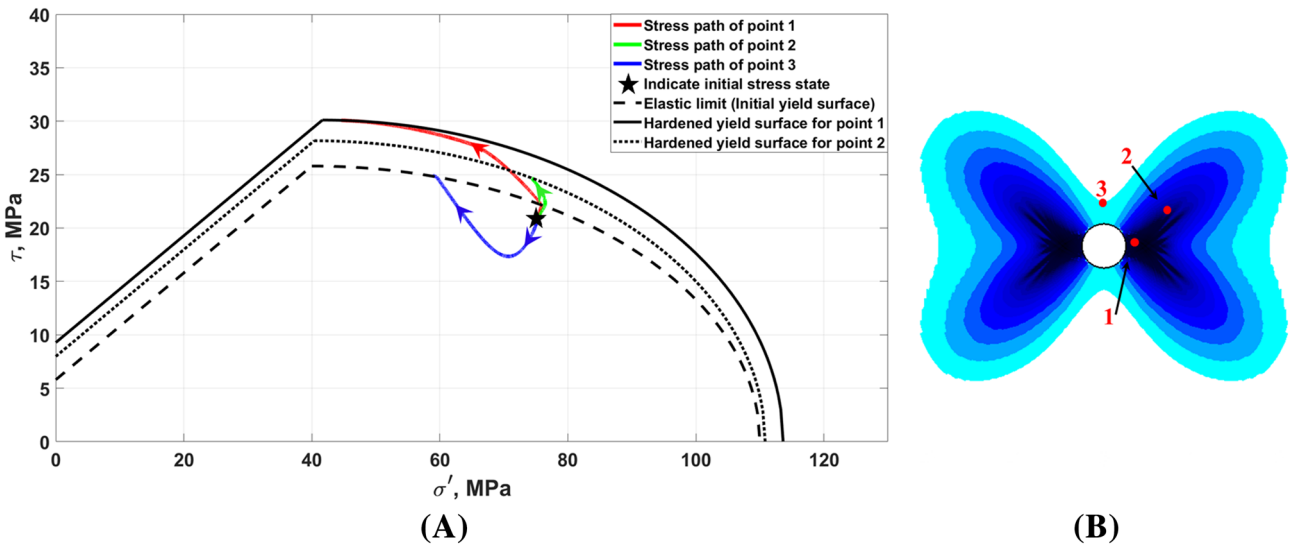


FIGURE 18 (a) Stress paths of the selected points and the corresponding yield surfaces and (b) configuration of the plastic zone and the position of investigated points

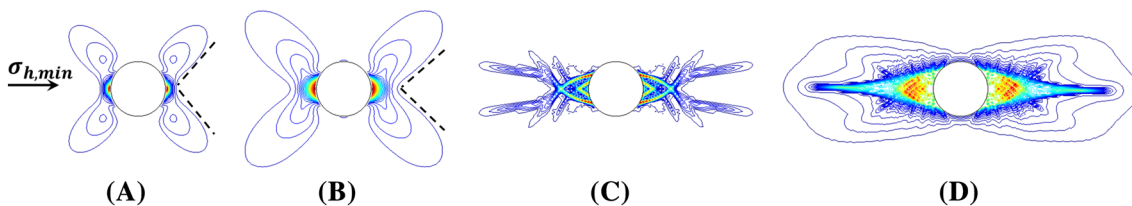


FIGURE 19 Schematic of different plastic zone configurations under, (a) shear-induced dilation and (b-d) shear-enhanced compaction mechanisms

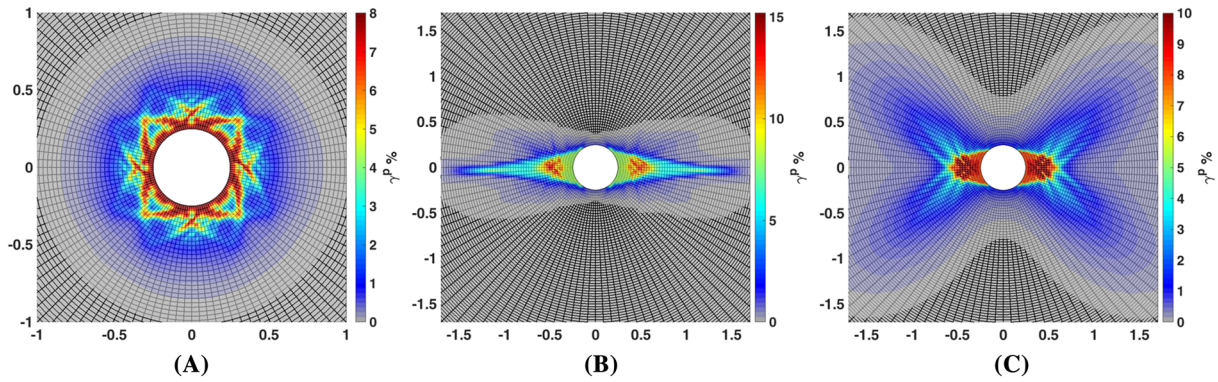
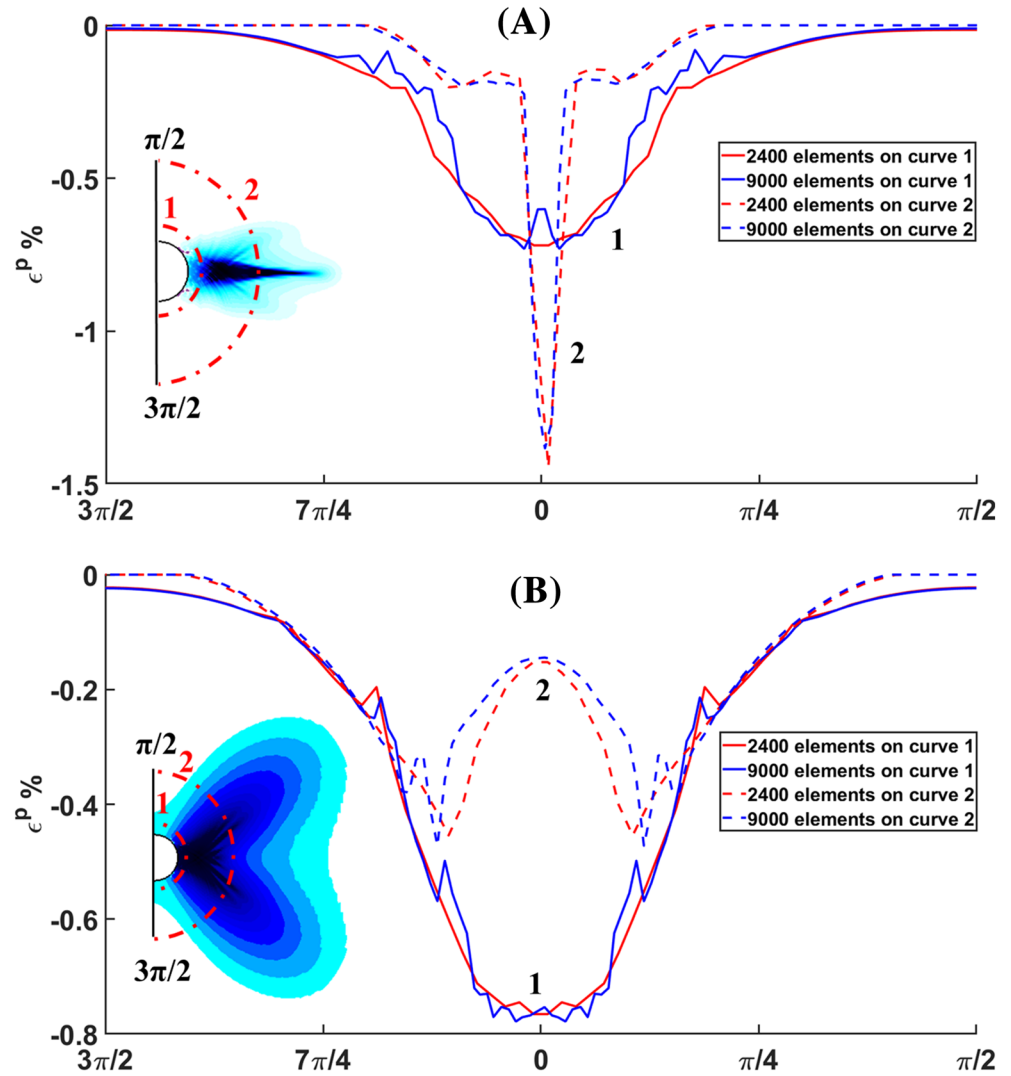


FIGURE 20 The accumulated inelastic equivalent shear strain using 2400 elements in one-quarter of computational domain with the same conditions as in (a) Figure 10b, (b) Figure 11b, and (c) Figure 12b with 9000

FIGURE 21 Inelastic volumetric strain variation around the wellbore using different domain meshing (a) needle-shaped and (b) butterfly-shaped localization patterns



the figures because the magnitude of the positive volume deformation can be much less than the negative value. This fact is seen in the presented Figures 14, 15, and 17, as evidenced by the scale of inelastic volumetric strain values. Therefore, often around the wellbore, there is an alternation of dilatancy-compaction-dilatancy zones. Due to the fact that the most frequent deformation is the mixed mode, in which both dilatancy and compaction zones are formed, the breakout region can take an intricate form. The inelastic volumetric strain on the presented results is within the range

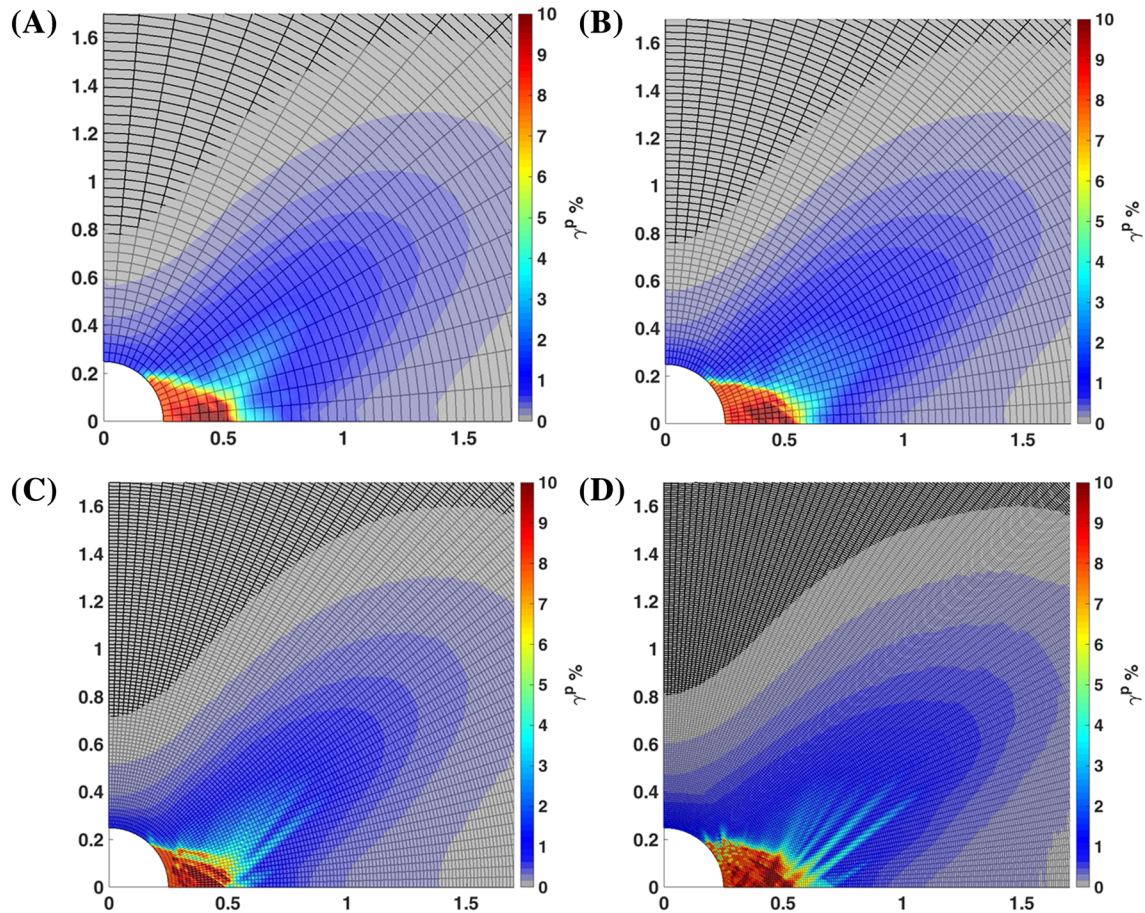


FIGURE 22 The accumulated inelastic equivalent shear strain for the same condition as in Figure 12 with (a) 1080, (b) 2400, (c) 9000, and (d) 22500 elements (the one-quarter of the computational domain is represented to clearly demonstrate the mesh size)

of 1-2.5%. Considering this roughly as a change in porosity, there would be a consequent change in microstructure and the fluid flow properties of the rock. Using the Kozeny-Carman equation, which represents permeability variation versus porosity and microstructure parameters, the permeability alteration near-wellbore zone can be estimated approximately.⁷² This permeability variation around the wellbore, especially in compaction mode can significantly affect the expected production rate and leads to fallacious predictions and planning.

Figure 16 represents the stress paths of the selected points and the corresponding yield surfaces for the needle-shaped plastic zone configuration. It can be seen that stress path due to drilling operation for points 1 and 2, which are located parallel to the minimum horizontal stress is accompanied by an increase in the deviatoric stress. As stress paths reach to elastic yield limit, the hardening stage is followed by a decrease in mean stress. On the other hand, the stress path of point 3 initially descends, and then continues to ascend with the increase in deviator stress and the decrease in mean stress. It is important to note that the initial stress state and the pressure inside wellbore (P_w) control the local stress paths around the wellbore in the elastic region. As the stress path reaches the elastic yield surface, the parameters of the constitutive model determine the further path of stress.

Similar to Figure 16, Figure 18 represents the stress paths of the selected points and the corresponding yield surfaces for the butterfly-shaped plastic zone configuration. For this case, the initial stress state is just next to the elastic yield surface. As stress in points 1 and 2 reaches the elastic limit, their corresponding yield surfaces are expanded with different expansion speeds. A comparison of the local stress paths in the vicinity of wellbore discussed above may help explain the dependence of plastic deformation patterns on the far-field stresses and stress paths.

Finally, it is important to indicate that the simulations of irreversible deformation around the wellbore are not strongly mesh-dependent, and, with changing mesh size, these zones preserve their general characteristics. As previously explained, the mesh-dependency exists, but, regarding solving the dynamic equations with a small increment in

the loads, the form of irreversible deformation zones preserved. The form of irreversible deformations is controlled by the constitutive equations and the stress state.

Figure 20 shows the results of strain localization, obtained with the same conditions as in figures 14, 15, and 17 but with the different discretization of the domain around the wellbore (2400 elements in one-quarter of the computational domain). Based on figure 20, the general form and characteristics of localization zones are very similar to those obtained in figures 14, 15, and 17. Figure 21 shows the quantitative variation of inelastic volumetric deformation of needle and butterfly patterns on two arches around the wellbore for two different mesh sizes. As seen, the finer mesh encompasses the wider range and, in more detail, the irreversible deformation process. At the same time, it maintains the trend and general characteristics of the plastic zone. Figure 22 represents the results in terms of mesh dependency, obtained with the same boundary conditions as in figure 17. As can be seen, all meshes predict a very similar localization pattern.

5 | CONCLUSION

The simulation of the deformation process around the wellbore in the drilling stage showed an irreversible deformation with an evolution of the localization zone with a subsequent failure zone. The regime of irreversible deformation and the shape of the failure region depend on the initial stress state of the medium, its mechanical properties, and the pressure of the drilling fluid. Most often in highly porous rocks, the development of irreversible deformation occurs in a mixed-mode when there are regions of compaction and dilatancy zones. Each deformation regime has certain consequences.

If the porosity and permeability of the rock are highly dependent on inelastic volumetric strain, in order to maintain the shape of the well and prevent failure, it is crucial that the magnitude of the accumulated inelastic equivalent shear strain does not exceed a critical value when the softening process begins, which quickly ends in failure. A more realistic approach would be to search for conditions under which localization of the deformation does not lead to the formation of considerable breakouts. Since the regimes and the size of the irreversible deformation depend on the effective stresses, the change in the pore pressure can have a significant effect on the further development of the process. Therefore, through meticulous selection of optimum mud pressure, it is possible to control the nature of deformation development.

The scheme of the dependence of the configuration of the zone of irreversible deformation on the loading conditions is constructed. Such a scheme can be useful for choosing the optimal drilling modes and also explaining the observed phenomena during drilling and exploitation. Not only the flow rate but also the stability of the wellbore, as well as sanding problems, depends on the development modes and the magnitude of the deformation. During the compaction as a result of the removal of particles, the uncontrolled destruction of the rock around the wellbore is possible.

The proposed numerical approach can simultaneously compute the deformations in both shear-induced dilation in the brittle regime and shear-enhanced compaction in the cataclastic regime. The prediction of plastic deformation in compaction mode provides the opportunity for evaluating the possible source of sand production, changing fluid flow path and capacity in the near-wellbore zone and producing mechanism of the reservoir. Another remarkable outcome of the numerical analysis is the calculation of stress concentration at the tip of breakouts. An increase in effective stresses at the tip of breakouts can lead to a change in the regime of irreversible deformation from the dilatancy to the compaction mode, in which crushing and repacking of the grains occur.

ORCID

Aboozar Garavand  <https://orcid.org/0000-0001-7859-7984>

REFERENCES

1. Al-Ajmi AM, Zimmerman RW. Stability analysis of vertical boreholes using the Mogi–Coulomb failure criterion. *Int J Rock Mech Min Sci*. 2006;43(8):1200-1211.
2. Ewy RT. Wellbore-stability predictions by use of a modified Lade criterion. 1999.
3. Fjær E, Ruistuen H. Impact of the intermediate principal stress on the strength of heterogeneous rock. *J Geophys Res Solid Earth*. 2002; 107:ECV 3-1-ECV 3-10.
4. Haimson B, Chang C. A new true triaxial cell for testing mechanical properties of rock, and its use to determine rock strength and deformability of Westerly granite. *Int J Rock Mech Min Sci*. 2000;37(1-2):285-296.
5. Mogi K. Fracture and flow of rocks under high triaxial compression. *J Geophys Res*. 1971;76(5):1255-1269.

6. Kirsch EG. Die Theorie der Elastizität und die Bedürfnisse der Festigkeitslehre. *Zeitschrift des Vereines deutscher Ingenieure*. 1898;42: 797-807.
7. Bradley WB. Failure of inclined boreholes. *J Energy Resour Technol*. 1979;101(4):232-239.
8. Baud P, Vajdova V, Wong TF. Shear-enhanced compaction and strain localization: inelastic deformation and constitutive modeling of four porous sandstones. *J Geophys Res Solid Earth*. 2006;111(B12):1-17.
9. Das A, Buscarnera G. Simulation of localized compaction in high-porosity calcarenite subjected to boundary constraints. *Int J Rock Mech Min Sci*. 2014;71:91-104.
10. Fortin J, Schubnel A, Guéguen Y. Elastic wave velocities and permeability evolution during compaction of Bleurswiller sandstone. *Int J Rock Mech Min Sci*. 2005;42:873-889.
11. Fortin J, Stanchits S, Dresen G, Guéguen Y. Acoustic emission and velocities associated with the formation of compaction bands in sandstone. *J Geophys Res Solid Earth*. 2006;111(B10):1-16.
12. Fossen H, Schultz RA, Shipton ZK, Mair K. Deformation bands in sandstone: a review. *J Geol Soc London*. 2007;164:755-769.
13. Issen KA, Rudnicki JW. Conditions for compaction bands in porous rock. *J Geophys Res Solid Earth*. 2000;105:21529-21536.
14. Nguyen S-H, Chemenda AI, Ambre J. Influence of the loading conditions on the mechanical response of granular materials as constrained from experimental tests on synthetic rock analogue material. *Int J Rock Mech Min Sci*. 2011;48:103-115.
15. Olsson WA. Theoretical and experimental investigation of compaction bands in porous rock. *J Geophys Res Solid Earth*. 1999;104:7219-7228.
16. Stefanov YP, Chertov MA, Aidagulov GR, Myasnikov AV. Dynamics of inelastic deformation of porous rocks and formation of localized compaction zones studied by numerical modeling. *J Mech Phys Solids*. 2011;59:2323-2340.
17. Wong TF, David C, Zhu W. The transition from brittle faulting to cataclastic flow in porous sandstones: mechanical deformation. *J Geophys Res Solid Earth*. 1997;102:3009-3025.
18. Galin LA. Plane elastoplastic problem. Plastic regions at a circular hole in plates and beams. *Prikl Mat Mekh*. 1946;10:367-386.
19. Savin GN. *Stress distribution around holes*. Oxford, United Kingdom: Pergamon press; 1970.
20. Ostrosablin NP. Plastic zone around a round hole in a plane with a nonuniform basic stressed state. *Journal of Applied Mechanics and Technical Physics*. 1990;31:783-792.
21. Zhou H, Kong G, Liu H. A semi-analytical solution for cylindrical cavity expansion in elastic-perfectly plastic soil under biaxial in situ stress field. *Géotechnique*. 2016;66:584-595.
22. Detournay E. An approximate statical solution of the elastoplastic interface for the problem of Galin with a cohesive-frictional material. *International Journal of Solids and Structures*. 1986;22:1435-1454.
23. Bradford IDR, Cook JM. A semi-analytic elastoplastic model for wellbore stability with applications to sanding. *Rock Mechanics in Petroleum Engineering*. 1994:347-354. <https://doi.org/10.2118/28070-MS>
24. Fung LSK, Wan RG, Rodriguez H, Bellorin IRS. An advanced elasto-plastic model for borehole stability analysis of horizontal wells in unconsolidated formation. *Annual Technical Meeting*. 1996:1-21. <https://doi.org/10.2118/96-58>
25. Rudnicki JW. Shear and compaction band formation on an elliptic yield cap. *J Geophys Res Solid Earth*. 2004;109:1-10.
26. Grueschow E, Rudnicki JW. Elliptic yield cap constitutive modeling for high porosity sandstone. *International Journal of Solids and Structures*. 2005;42:4574-4587.
27. Dimaggio FL, Sandler IS. Material model for granular soils. *J Eng Mech*. 1971;79:935-950.
28. Das A, Tengattini A, Nguyen GD, Viggiani G, Hall SA, Einav I. A thermomechanical constitutive model for cemented granular materials with quantifiable internal variables. Part II – validation and localization analysis. *J Mech Phys Solids*. 2014;70:382-405.
29. Mas D, Chemenda AI. An experimentally constrained constitutive model for geomaterials with simple friction-dilatancy relation in brittle to ductile domains. *Int J Rock Mech Min Sci*. 2015;77:257-264.
30. Chemenda AI, Mas D. Dependence of rock properties on the Lode angle: experimental data, constitutive model, and bifurcation analysis. *J Mech Phys Solids*. 2016;96:477-496.
31. Ortiz M, Leroy Y, Needleman A. A finite element method for localized failure analysis. *Comput Methods Appl Mech Eng*. 1987;61: 189-214.
32. Borja Ronaldo I, Regueiro Richard A, Lai TY. FE Modeling of strain localization in soft rock. *J Geotech Geoenviron Eng*. 2000;126: 335-343.
33. Simo JC, Oliver J, Armero F. An analysis of strong discontinuities induced by strain-softening in rate-independent inelastic solids. *Computational Mechanics*. 1993;12:277-296.
34. Shahin G, Desrues J, Pont SD, Combe G, Argilaga A. A study of the influence of REV variability in double-scale FEM × DEM analysis. *Int J Numer Methods Eng*. 2016;107:882-900.
35. Guo N, Zhao J. 3D multiscale modeling of strain localization in granular media. *Computers and Geotechnics*. 2016;80:360-372.
36. Wu H, Zhao J, Guo N. Multiscale insights into borehole instabilities in high-porosity sandstones. *J Geophys Res Solid Earth*. 2018;123: 3450-3473.
37. Desrues J, Argilaga A, Caillerie D, et al. From discrete to continuum modelling of boundary value problems in geomechanics: an integrated FEM-DEM approach. *International Journal for Numerical and Analytical Methods in Geomechanics*. 2019;43:919-955.
38. Biot MA. Theory of propagation of elastic waves in a fluid-saturated porous solid. *I Low-frequency range The Journal of the Acoustical Society of America*. 1956;28:168-178.
39. Biot MA. General Theory of Three-Dimensional Consolidation. *J Appl Phys*. 1941;12:155-164.

40. Biot MA. Theory of propagation of elastic waves in a fluid-saturated porous solid. II Higher frequency range *The Journal of the Acoustical Society of America*. 1956;28:179-191.
41. Yarushina VM, Podladchikov YY. (De)compaction of porous viscoelastoplastic media: model formulation. *J Geophys Res Solid Earth*. 2015;120:4146-4170.
42. Rice JR, Cleary MP. Some basic stress diffusion solutions for fluid-saturated elastic porous media with compressible constituents. *Rev Geophys*. 1976;14:227-241.
43. Carslaw HS, Jaeger JC. *Conduction of heat in solids*. Oxford: Clarendon Press; 1959.
44. Drucker DC, Prager W. Soil mechanics and plastic analysis or limit design. *Quarterly of Applied Mathematics*. 1952;10:157-165.
45. Nikolaevskii VN. Governing equations of plastic deformation of a granular medium. *Journal of Applied Mathematics and Mechanics*. 1971;35:1017-1029.
46. Nikolaevskii VN. Mechanical properties of soils and plasticity theory. In: *Solid Mechanics*. 1972;6:5-85.
47. Rudnicki JW, Rice JR. Conditions for the localization of deformation in pressure-sensitive dilatant materials. *J Mech Phys Solids*. 1975; 23(6):371-394.
48. Issen KA, Rudnicki JW. Theory of compaction bands in porous rock. *Physics and Chemistry of the Earth, Part A: Solid Earth and Geodesy*. 2001;26:95-100.
49. Baud P, Schubnel A, Wong T. Dilatancy, compaction, and failure mode in Solnhofen limestone. *J Geophys Res Solid Earth*. 2000;105: 19289-19303.
50. Vajdova V, Baud P, Wong TF. Compaction, dilatancy, and failure in porous carbonate rocks. *J Geophys Res Solid Earth*. 2004;109:1-16.
51. Stefanov YP. Deformation localization and fracture in geomaterials. *Numerical simulation Journal of Phys Mesomech*. 2002;5:107-118.
52. Wilkins ML. *Computer simulation of dynamic phenomena*. New York, Inc: Springer-Verlag; 1998.
53. Wilkins ML. *Calculation of elastic-plastic flow*. Livermore, CA: University of California Lawrence Radiation Laboratory; 1963.
54. Wilkins ML. Use of artificial viscosity in multidimensional fluid dynamic calculations. *J Comput Phys*. 1980;36:281-303.
55. Cundall PA. Distinct element models of rock and soil structure. *Analytical and Computational Methods in Engineering Rock Mechanics* 1987, ch. 4:129-163.
56. Poliakov ANB, Cundall PA, Podladchikov YY, Lyakhovsky VA. An explicit inertial method for the simulation of viscoelastic flow: an evaluation of elastic effects on diapiric flow in two- and three-layers models. In: Stone DB, Runcorn SK, eds. *Flow and creep in the Solar System: observations, modeling and theory*. Dordrecht: Springer Netherlands; 1993:175-195.
57. Zimmerman RW, Somerton WH, King MS. Compressibility of porous rocks. *J Geophys Res Solid Earth*. 1986;91(B12):12765-12777.
58. Baud P, Reuschlé T, Ji Y, Cheung CSN, Wong T-F. Mechanical compaction and strain localization in Bleurswiller sandstone. *J Geophys Res Solid Earth*. 2015;120:6501-6522. <https://doi.org/10.1002/2015JB012192>
59. Heap MJ, Brantut N, Baud P, Meredith PG. Time-dependent compaction band formation in sandstone. *J Geophys Res Solid Earth*. 2015; 120:4808-4830.
60. Baud P, Klein E, T-f W. Compaction localization in porous sandstones: spatial evolution of damage and acoustic emission activity. *Journal of Structural Geology*. 2004;26:603-624.
61. Shahin G, Buscarnera G. Numerical simulation of localized compaction creep in heterogeneous porous rock. *53rd US Rock Mechanics/ Geomechanics Symposium*. 2019;1-7. Available at: <https://doi.org/>
62. Shahin G, Marinelli F, Buscarnera G. Viscoplastic interpretation of localized compaction creep in porous rock. *J Geophys Res Solid Earth*. 2019;124:10180-10196. <https://doi.org/10.1029/2019JB017498>
63. Peerlings RHJ, De Borst R, Brekelmans WAM, De Vree JHP. Gradient enhanced damage for quasi-brittle materials. *Int J Numer Methods Eng*. 1996;39:3391-3403.
64. De Borst R. Fundamental issues in finite element analyses of localization of deformation. *Engineering Computations*. 1993;10:99-121.
65. Zienkiewicz OC, Taylor RL, Zhu JZ. *The finite element method set (Sixth Edition)*. 2 Oxford: Butterworth-Heinemann; 2005:xiii-xv.
66. Zoback MD, Moos D, Mastin L, Anderson RN. Well bore breakouts and in situ stress. *J Geophys Res Solid Earth*. 1985;90:5523-5530.
67. Vernik L, Zoback MD. Estimation of maximum horizontal principal stress magnitude from stress-induced well bore breakouts in the Cajon Pass Scientific Research borehole. *J Geophys Res Solid Earth*. 1992;97:5109-5119.
68. Haimson B. Micromechanisms of borehole instability leading to breakouts in rocks. *Int J Rock Mech Min Sci*. 2007;44:157-173.
69. Spiezia N, Salomoni VA, Majorana CE. Plasticity and strain localization around a horizontal wellbore drilled through a porous rock formation. *International Journal of Plasticity*. 2016;78:114-144.
70. Marinelli F, Buscarnera G. Parameter calibration for high-porosity sandstones deformed in the compaction banding regime. *Int J Rock Mech Min Sci*. 2015;78:240-252.
71. Stefanov Yu P, Bakeev RA. Formation of dilation and compaction zones around wells. *AIP Conf Proc*. 2014;1623:619-622.
72. Mavko G, Nur A. The effect of a percolation threshold in the Kozeny-Carman relation. *Geophysics*. 1997;62:1480-1482.
73. Hiramatsu Y, Oka Y. Determination of the stress in rock unaffected by boreholes or drifts, from measured strains or deformations. *International Journal of Rock Mechanics and Mining Sciences & Geomechanics Abstracts*. 1968;5:337-353.

How to cite this article: Garavand A, Stefanov YP, Rebetsky YL, Bakeev RA, Myasnikov AV. Numerical modeling of plastic deformation and failure around a wellbore in compaction and dilation modes. *Int J Numer Anal Methods Geomech*. 2020;1–28. <https://doi.org/10.1002/nag.3041>

APPENDIX A

5.1 | MODIFICATION OF THE 2D PLANE STRAIN CONDITION BY IMITATING THIRD STRESS IN NUMERICAL SCHEME

In some practical applications, it is a good approximation to assume that along with a certain axis all cross-sections are in the same condition and there is no displacement along the axis. This state of strain is called plane strain that is commonly used in 2D numerical simulations and can be expressed in polar coordinates as:

$$\varepsilon_{zz} = 0, \quad (\text{A1})$$

$$\sigma_{zz} = \nu(\sigma_{rr} + \sigma_{\theta\theta}). \quad (\text{A2})$$

This means that the third stress (σ_{zz}) for isotropic media only depends on Poisson's ratio and on stresses in the plane. However, for petroleum industry purposes, it is necessary to consider the full state of stress (one vertical and two horizontals) for which the approximate values are known.

Inspiring from the work of Hiramatsu et al,⁷³ we assume that the plane is loaded with additional axial stress (σ_v), and the initial stress state is in an equilibrium condition (before drilling). Then, assuming that after drilling the plane strain condition is still satisfied along the wellbore axis (assuming that the cylinder is infinitely long), we can write the increment of strain in the z-direction as follows:

$$d\varepsilon_{zz} = \frac{1}{E}[d\sigma_{zz} - \nu(d\sigma_{rr} + d\sigma_{\theta\theta})]. \quad (\text{A3})$$

Under the plane strain assumption ($d\varepsilon_{zz}=0$), we obtain the following expression for the increment of stress along the normal of the plane as:

$$d\sigma_{zz} = \nu(d\sigma_{\theta\theta} + d\sigma_{rr}). \quad (\text{A4})$$

Therefore, the final stress in the z-direction is computed by adding the increment of stress due to drilling under the plane strain condition to the initial acting stress (σ_v) as:

$$\sigma_{zz} = \sigma_v + d\sigma_{zz} = \sigma_v + \nu(d\sigma_{\theta\theta} + d\sigma_{rr}). \quad (\text{A5})$$

Including modified plane strain (A5) instead of the classical form of plane strain (A2) in the 2D numerical scheme allows us to simulate full stress state in two-dimensional problems.

For an isotropic medium (see Figure A1) constrained by the depicted boundary conditions, by transforming Cartesian to cylindrical coordinates, the following expressions can be easily found for the applied stresses:

$$\sigma_{\theta\theta}^0 = 1/2[(\sigma_{xx} + \sigma_{yy}) - (\sigma_{xx} - \sigma_{yy})\cos 2\theta], \quad (\text{A6})$$

$$\sigma_{rr}^0 = 1/2[(\sigma_x + \sigma_y) + (\sigma_x - \sigma_y)\cos 2\theta]. \quad (\text{A7})$$

According to Kirsch⁶, drilling a borehole in this medium leads to the redistribution of tangential and radial stresses which can be stated as follows:

$$\sigma_{\theta\theta}^1 = \frac{1}{2}(\sigma_{xx} + \sigma_{yy})\left(1 + \frac{R_w^2}{r^2}\right) - \frac{1}{2}(\sigma_{xx} - \sigma_{yy})\left(1 + \frac{3R_w^4}{r^4}\right)\cos 2\theta - \sigma_{xy}\left(1 + \frac{3R_w^4}{r^4}\right)\sin 2\theta - P_w \frac{R_w^2}{r^2}, \quad (\text{A8})$$

$$\sigma_{rr}^1 = \frac{1}{2}(\sigma_{xx} + \sigma_{yy})\left(1 - \frac{R_w^2}{r^2}\right) + \frac{1}{2}(\sigma_{xx} - \sigma_{yy})\left(1 - \frac{4R_w^2}{r^2} + \frac{3R_w^4}{r^4}\right)\cos 2\theta + \sigma_{xy}\left(1 - \frac{4R_w^2}{r^2} + \frac{3R_w^4}{r^4}\right)\sin 2\theta + P_w \frac{R_w^2}{r^2}. \quad (\text{A9})$$

Subtracting expressions (A8, A9) from (A6, A7) respectively, and inserting the results in (A5), we obtain the following expression for the final stress along the normal of the plane as:

$$\sigma_{zz} = \sigma_v - \nu \left[2(\sigma_{xx} - \sigma_{yy}) \frac{R_w^2}{r^2} \cos 2\theta + 4\sigma_{xy} \frac{R_w^2}{r^2} \sin 2\theta \right], \quad (A10)$$

which coincides with the solution of 3D analytical solution.

Figure A2 illustrates the results of the above modification applied in numerical algorithm computed for three different stress conditions ($\sigma_v=10, 30,$ and 60 MPa) and the results obtained in the classical form of plane strain, compared to their respective 3D analytical solutions. The excellent coincidence of numerical and analytical results proves the validity of our approach to modifying the accustomed plane strain method and can be considered as a pseudo-3D plane strain model.

According to Figure A3, for the above-mentioned stress conditions, stress paths from the initial state of stress to the final state are absolutely different, which may even lead to different failure mechanisms. For example, stress path ¹ results in the shear-induced dilation mechanism, while the expected failure mechanism for the stress path ³ is shear-enhanced compaction.

The above results demonstrate that neglecting the third acting stress might cause misinterpretation of 2D numerical simulation outcomes due to the experience of different stress paths.

FIGURE A1 Scheme of stress state before and after drilling operation

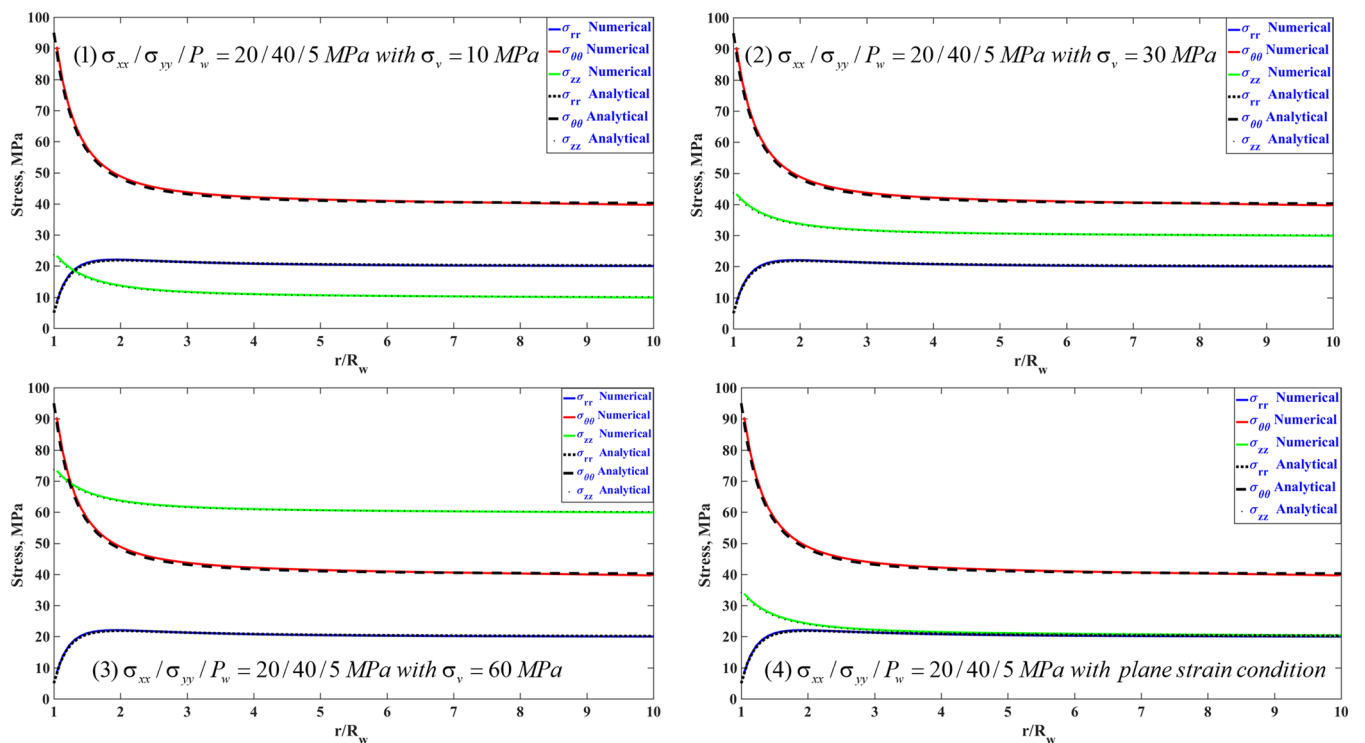
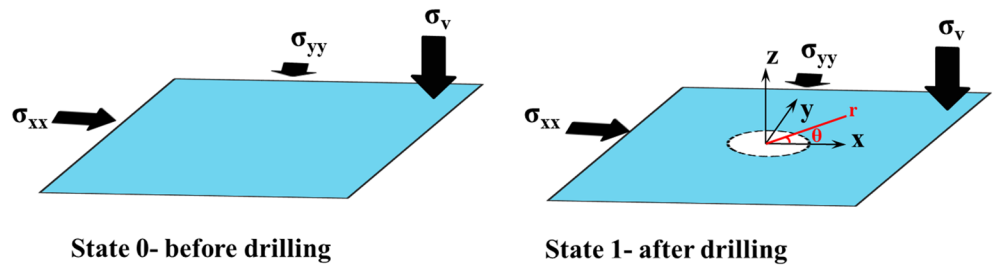


FIGURE A2 Comparison of pseudo-3D plane strain and plane-strain results using the numerical model versus 3D analytical solution

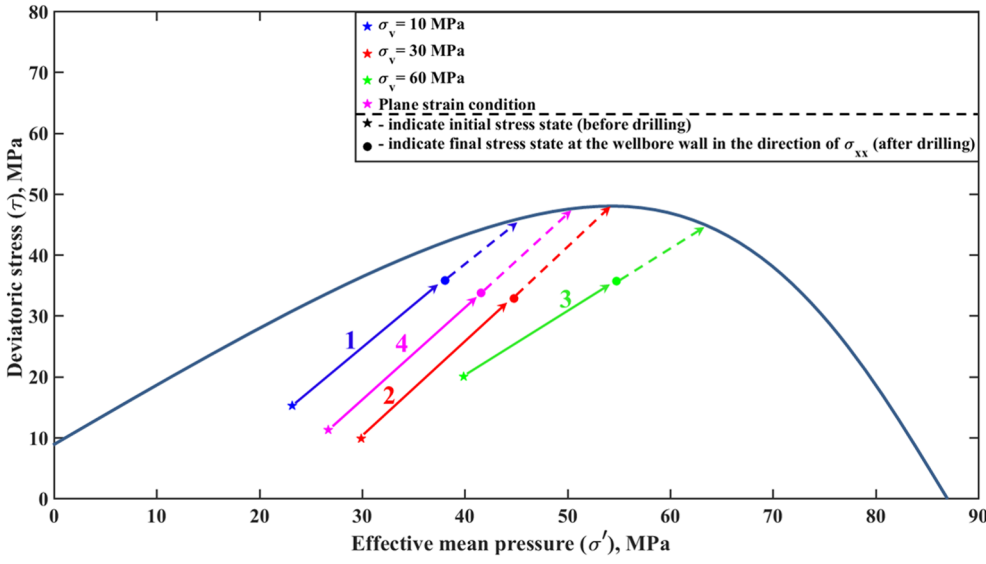


FIGURE A3 Stress paths under different conditions